The University of Maine
DigitalCommons@UMaine

Electronic Theses and Dissertations Fogler Library

12-2016

Investigating High Speed Localization Microscopy Through Experimental Methods, Data Processing Methods, and Applications of Localization Microscopy to Biological Questions

Andrew J. Nelson
University of Maine, andrew.j.nelson@maine.edu

Follow this and additional works at: http://digitalcommons.library.umaine.edu/etd

Part of the Artificial Intelligence and Robotics Commons, Biological and Chemical Physics Commons, Optics Commons, and the Virology Commons

Recommended Citation

Nelson, Andrew J., "Investigating High Speed Localization Microscopy Through Experimental Methods, Data Processing Methods, and Applications of Localization Microscopy to Biological Questions" (2016). *Electronic Theses and Dissertations*. 2530.
http://digitalcommons.library.umaine.edu/etd/2530

This Open-Access Dissertation is brought to you for free and open access by DigitalCommons@UMaine. It has been accepted for inclusion in Electronic Theses and Dissertations by an authorized administrator of DigitalCommons@UMaine.

The University of Maine
DigitalCommons@UMaine

Electronic Theses and Dissertations Fogler Library

12-2016

Investigating High Speed Localization Microscopy Through Experimental Methods, Data Processing Methods, and Applications of Localization Microscopy to Biological Questions

Andrew J. Nelson
University of Maine, andrew.j.nelson@maine.edu

Follow this and additional works at: http://digitalcommons.library.umaine.edu/etd

Part of the Artificial Intelligence and Robotics Commons, Biological and Chemical Physics Commons, Optics Commons, and the Virology Commons

Recommended Citation

Nelson, Andrew J., "Investigating High Speed Localization Microscopy Through Experimental Methods, Data Processing Methods, and Applications of Localization Microscopy to Biological Questions" (2016). *Electronic Theses and Dissertations*. 2530.
http://digitalcommons.library.umaine.edu/etd/2530

This Open-Access Dissertation is brought to you for free and open access by DigitalCommons@UMaine. It has been accepted for inclusion in Electronic Theses and Dissertations by an authorized administrator of DigitalCommons@UMaine.

INVESTIGATING HIGH SPEED LOCALIZATION MICROSCOPY THROUGH EXPERIMENTAL METHODS, DATA PROCESSING METHODS, AND APPLICATIONS OF LOCALIZATION MICROSCOPY TO BIOLOGICAL QUESTIONS

By

Andrew J. Nelson

B.S. College of William and Mary, 2010

A DISSERTATION

Submitted in Partial Fulfillment of the

Requirements for the Degree of

Doctor of Philosophy

(in Physics)

The Graduate School

The University of Maine

December 2016

Advisory Committee:

Samuel Hess, Professor of Physics, Advisor

Raymond Astumian, Professor of Physics

Robert Meulenberg, Associate Professor of Physics

George Bernhardt, Research Scientist

Paul Millard, Associate Professor of Chemical and Biological Engineering

DISSERTATION ACCEPTANCE STATEMENT

On behalf of the Graduate Committee for Andrew Nelson I affirm that this manuscript is the final and accepted dissertation. Signatures of all committee members are on file with the Graduate School at the University of Maine, 42 Stodder Hall, Orono, Maine.

Samuel Hess, Professor of Physics Date

Copyright 2016 Andrew Nelson

LIBRARY RIGHTS STATEMENT

In presenting this dissertation in partial fulfillment of the requirements for an advanced degree at The University of Maine, I agree that the Library shall make it freely available for inspection. I further agree that permission for “fair use” copying of this dissertation for scholarly purposes may be granted by the Librarian. It is understood that any copying or publication of this dissertation for financial gain shall not be allowed without my written permission.

Signature:

Date: 11/30/16

INVESTIGATING HIGH SPEED LOCALIZATION MICROSCOPY THROUGH EXPERIMENTAL METHODS, DATA PROCESSING METHODS, AND APPLICATIONS OF LOCALIZATION MICROSCOPY TO BIOLOGICAL QUESTIONS

By Andrew J. Nelson

Dissertation Advisor: Dr. Samuel Hess

An Abstract of the Dissertation Presented
in Partial Fulfillment of the Requirements for the
Degree of Doctor of Philosophy
(in Physics)
December 2016

Fluorescence Photoactivation Localization Microscopy(FPALM) and other super resolution localization microscopy techniques can resolve structures with nanoscale resolution. Unlike techniques of electron microscopy, they are also compatible with live cell and live animal studies, making FPALM and related techniques ideal for answering questions about the dynamic nature of molecular biology in living systems. Many processes in biology occur on rapid sub second time scales requiring the imaging technique to be capable of resolving these processes not just with a high enough spatial resolution, but with an appropriate temporal resolution. To that end, this Dissertation in part investigates high speed FPALM as an experimental technique showing images can be reconstructed with effective temporal resolutions of 0.1s. Using fluorescent proteins attached to an influenza viral protein, hemagglutinin(HA), questions of protein clustering and cluster dynamics on the host cell membrane are explored. The results indicate that these HA clusters may be more dynamic than previously thought. The principle disadvantage of the increased speed of imaging is the reduction in information that comes through collecting fewer photons to localize each molecule, and fewer molecules overall. As the molecules become dimmer, they also become harder to identify using conventional identification algorithms. Tools from machine learning and computer vision such as artificial neural networks(ANNs) have been shown to be adept at object identification. Here a method for repeatedly training an ANN is investigated. This method is shown to have exceptional performance on simulations indicating that it can be regarded as a method of high fidelity, even in the presence of weakly fluorescent molecules. Development of this technique can be used to recover more molecules from data sets with weaker molecular fluorescence, such as those obtained with high speed imaging, allowing for higher sampling, and overall higher spatial resolution of the final image. The combination of a high speed experimental technique coupled with a sensitive and robust identification algorithm allow FPALM and related techniques to probe questions of fast biological processes while limiting the sacrifice to spatial resolution inherent in high speed techniques.

DEDICATION

This Dissertation is dedicated to the late Professor John Michael Finn from the College of William and Mary. During my time as an undergraduate, Professor Finn helped showed me the joys of physics as well as being the first professor to engage and challenge my abilities in the classroom. In part because of the enthusiasm you showed me, I have been able to persevere through to this point. Thank you for the confidence and strength you helped teach me.

ACKNOWLEDGEMENTS

I wish to first thank Dr. Samuel T. Hess for his immeasurable contribution to my achievements in the years I spent at the University of Maine. His patience, guidance, and encouragement were always dearly appreciated. I also wish to thank my wife Desiree M. Nelson whose love, kindness, and patience gave me the strength to persevere through the hardest points of this program. My thanks to Shawn Brackett, Dahan Kim, Lisa Weatherly, Michael Brady Butler, Dr. Nikki Curthoys, Dr. Francesca Pennacchietti, Dr. Joshua Wright, Dr. Michael Mlodzianoski, Matthew Valles, Matthew Parent, Bryn Nugent, Nicholas Palestini, Michael Savino, Logan Boyd, Kat Daly, John Brosnan, Dr. Joshua Zimmerburg, Dr. Mudalige Gunewardene, Dr. Julie Gosse, Dr. Raymond Astumian, Dr. Robert Meulenberg, Dr. George Bernhardt, Dr. Paul Millard, Patricia Byard, and Burt Hopple. I finally thank everyone who was not specifically mentioned but still through either friendship, or guidance helped me to complete my program here at the University of Maine.

Table of Contents

DEDICATION iv

ACKNOWLEDGEMENTS v

LIST OF FIGURES ix

LIST OF EQUATIONS x

LIST OF ABBREVIATIONS xi

Chapter

1. LOCALIZATION MICROSCOPY: MAPPING CELLULAR DYNAMICS WITH SINGLE MOLECULES 1

1.1. Introduction 2

1.2. Experimental Concept 4

1.3. Probes Compatible with SRFLM 7

1.4. Advanced SRFLM Methodologies 9

1.4.1. Multiple Channel Imaging 9

1.4.2. Three-Dimensional Imaging 11

1.5. Spatial Resolution 13

1.6. Optimization of Image Acquisition 14

1.7. Live-Cell Compatibility 15

1.8. Going Faster: Improving Temporal Resolution 16

1.9. Future Directions 17

2. HIGH SPEED FLUORESCENCE PHOTOACTIVATION LOCALIZATION MICROSCOPY IMAGING.. 19

2.1. Results 19

2.2. Discussion 23

2.2.1. Cluster Dynamics 23

2.2.2. Limited Number of Detected Photons per Molecule per Frame 23

2.2.3. Fluorescence Background 24

2.2.4. Live-Cell Viability 25

2.2.5. Proper Sampling 26

3. MOLECULAR IMAGING WITH NEURAL TRAINING OF IDENTIFCATION ALGORITHM (MINuTIA) 27

3.1 Introduction 28

3.2 Methods 29

3.3 Results 36

3.4 Discussion 40

3.5 Summary and Conclusion 45

BIBLIOGRAPHY 47

APPENDIX A: VIRUS INFECTION 55

A.1 Super-Resolution Microscopy: Viruses Meet Their Match 55

A.2 Influenza Virus Hemagglutinin: The Versatile Membrane Protein Hijacking Your Cells 56

A.3 Influenza Hemagglutinin and Host Cell Actin: An Unhealthy Relationship? 57

A.4 Role of Gag in HIV Life Cycle... 58

A.5 Outlook 59

BIOGRAPHY OF THE AUTHOR 61

LIST OF FIGURES

Figure 1. Example of a Typical Superresolution Experiment ………………………………………….. 5

Figure 2. Typical High Speed FPALM Results ……………………………………………………………… 22

Figure 3. Example of The Learning Process ………………………………………………………….…… 31

Figure 4. Example of Artificial Neural Network Architecture ……………………………………….. 35

Figure 5. Performance Versus Hidden Layer Nodes ………………………………………………………. 37

Figure 6. Examples of Experimental and Simulated Histograms of Fitting Parameters …………………………………………………………………………………………….… 39

Figure 7. Examples of Simulated Data Sets ……………………………………………………………….. 41

Figure 8. Results of Simulation …………………………………………………………………………….… 43

LIST OF EQUATIONS

Equation 1. Diffraction Limit 1
Equation 2. Anisotropy Equation 11
Equation 3. Logarithmic Cost Function 32
Equation 4. Hidden Layer Sigmoid Argument 33
Equation 5. Hidden Layer Unit Activation Value 33
Equation 6. Output Layer Sigmoid Argument 33
Equation 7. Output Layer Activation Value 33

LIST OF ABBREVIATIONS

SRFLM	Super Resolution Fluorescence Localization Microscopy
PSF	Point Spread Function
FPALM	Fluorescence Photoactivation Localization Microscopy
PALM	Photoactivated Localization Microscopy
STORM	Stochastic Optical Reconstruction Microscopy
ANN	Artificial Neural Network
MINuTIA	Molecular Identification by Neural Training of Identification Algorithm

CHAPTER 1

LOCALIZATION MICROSCOPY: MAPPING CELLULAR DYNAMICS WITH SINGLE MOLECULES

The following chapter is reproduced from the published article by Nelson and Hess, 2014[1].

Resolution describes the smallest details within a sample that can be recovered by a microscope lens system. For optical microscopes detecting visible light, diffraction limits the resolution to ∼200-250 nm. In contrast, localization measures the position of an isolated object using its image. Single fluorescent molecules can be localized with an uncertainty of a few tens of nanometres, and in some cases less than one nanometre. Superresolution fluorescence localization microscopy(SRFLM) images and localizes fluorescent molecules in a sample. By controlling the visibility of the fluorescent molecules with light, it is possible to cause a sparse subset of the tags to fluoresce and be spatially separated from each other. A movie is acquired with a camera, capturing images of many sets of visible fluorescent tags over a period of time. The movie is then analyzed by a computer whereby all of the single molecules are independently measured, and their positions are recorded. When the coordinates of a sufficient number of molecules are collected, an image can be rendered by plotting the coordinates of the localized molecules. The spatial resolution of these rendered images can be better than 20 nm, roughly an order of magnitude better than the diffraction limited resolution. The invention of SRFLM has led to an explosion of related techniques. Through the use of specialized optics, the fluorescent signal can be split into multiple detection channels. These channels can capture additional information such as color(emission wavelength), orientation and three-dimensional position of the detected molecules. Measurement of the color of the detected fluorescence can allow researchers to distinguish multiple types of fluorescent tags and to study the interaction between multiple molecules of interest. Three-dimensional imaging and determination of molecular orientations offer insight into structural organization of the sample. SRFLM is compatible with living samples and has helped to illuminate many dynamic biological processes, such as the trajectories of molecules within living cells. This review discusses the concept and process of SRFLM imaging and investigates recent advances in SRFLM functionality. Since its announcement in 2006, SRFLM has been quickly adopted and modified by many researchers to help investigate questions whose answers lie below the diffraction limit. The versatility of the SRFLM technique has great promise for improving our understanding of cell biology at the molecular level.

1.1. Introduction

Since the 17th century, biological specimens have been observed with the light microscope. The advantages of highly specific labeling and excellent sensitivity have made fluorescence one of the most popular types of light microscopy used to image biological systems. Compared to widefield fluorescence imaging, confocal fluorescence microscopy has improved spatial resolution and signal-to-background ratio, but both methods share a fundamental limitation in spatial resolution due to diffraction. The Rayleigh criterion specifies the minimum distance between two point sources as the distance from the center to the first minimum in the point spread function(PSF), which is given as

$$d = \frac{0.61\lambda}{NA} \tag{1}$$

where NA is the numerical aperture and λ is the emitted wavelength of light, and 0.61 is the value associated with the first diffraction minimum of the PSF, resulting in d~200-250 nm for a high-NA objective lens imaging visible light, and preventing structures smaller than d from being imaged with conventional methods.

Recently, SRFLM has circumvented the diffraction limit, enabling quantification of protein dynamics and biological structures at the molecular level in fixed and in vivo samples. The three seminal techniques of SRFLM are named Fluorescence Photoactivation Localization Microscopy(FPALM) [2], Photoactivatable Localization Microscopy(PALM) [3], and Stochastic Optical Reconstruction Microscopy(STORM) [4], Combined with the recently announced video rate acquisition[5], SRFLM has allowed researchers to image biological order on length scales inaccessible to the confocal microscope, and time scales inaccessible to the electron microscope.

While diffraction limits the minimum distance between two resolved objects, it does not limit how well an individual object can be localized; localization finds the location of an object using its image. Localization algorithms exist for determining locations of multiple objects in close proximity, but for the case of a single object in isolation, the process of localization involves simply fitting the recorded image of the object using the point spread function(PSF) or an approximation thereof. Localization of individual molecules has been published previously [6], and the precision with which an object can be localized has been quantified for a Gaussian fitting function by Thompson et al. [7]. Key factors determining the localization precision are the width of the PSF(related to the diffraction limited resolution), the total number of photons detected from the object, the background noise per pixel, and the effective camera pixel size. Former work has demonstrated measured localization precision close to one nanometer [8].

Fluorescent molecules make transitions between states, and the rates of such transitions can be controlled with light. Recent work has demonstrated that individual molecules will enter and exit states with different emission rates, either spontaneously or as a result of excitation by light. For example, organic dyes have been shown to undergo blinking and flicker and can be imaged at the single molecule level. It has also been shown that fluorescent proteins can also blink and flicker [9, 10]. Flicker occurs on short time scales ~ 0.1-0.5 ms and occurs when the chromophore of the protein shifts from a protonated non-fluorescent state, to a deprotonated fluorescent state. Blinking occurs when the fluorescent protein relaxes from the excited state, to a long lived non-fluorescent state. From this state, the protein can be optically driven back into the fluorescently active state and re-excited. The discovery of fluorescent blinking has allowed development of mechanisms to control the number of fluorescent proteins visible within a given field of view: photoactivatable fluorescent proteins(PAFPs)[11] are initially in a dark(non-fluorescent) state(within a particular spectral window) and can be converted with one wavelength into a form which is fluorescent under excitation by that same wavelength or another wavelength. Photoswitchable fluorescent proteins(PSFPs) emit initially in one wavelength range, and can be converted by light into a form which emits in a different wavelength range [12].

1.2. Experimental Concept

By exploiting the molecular photophysics, one can use time to separate otherwise overlapping PSFs, localize multiple sparse subsets of molecules, and combine all subsets to generate a superresolution image. To perform a SRFLM experiment, one must first prepare a sample by labeling proteins of interest with appropriate fluorescent probes. The fluorescent protein needs to have the ability to occupy a dark(non-fluorescent state), either by being photoactivatable or capable of blinking. Figure 1 demonstrates the corresponding experimental technique and data analysis using a photoactivatable fluorescent probe. By illuminating the labeled sample with an activation laser, with wavelength and intensity appropriate for the fluorescent probe, it is possible to cause the probes to switch from their dark state to an activated state stochastically. In this activated state the probes are illuminated by a secondary readout laser of specific wavelength and intensity, which causes the probes to emit fluorescence

FIGURE 1 Example of a Typical Superresolution Experiment

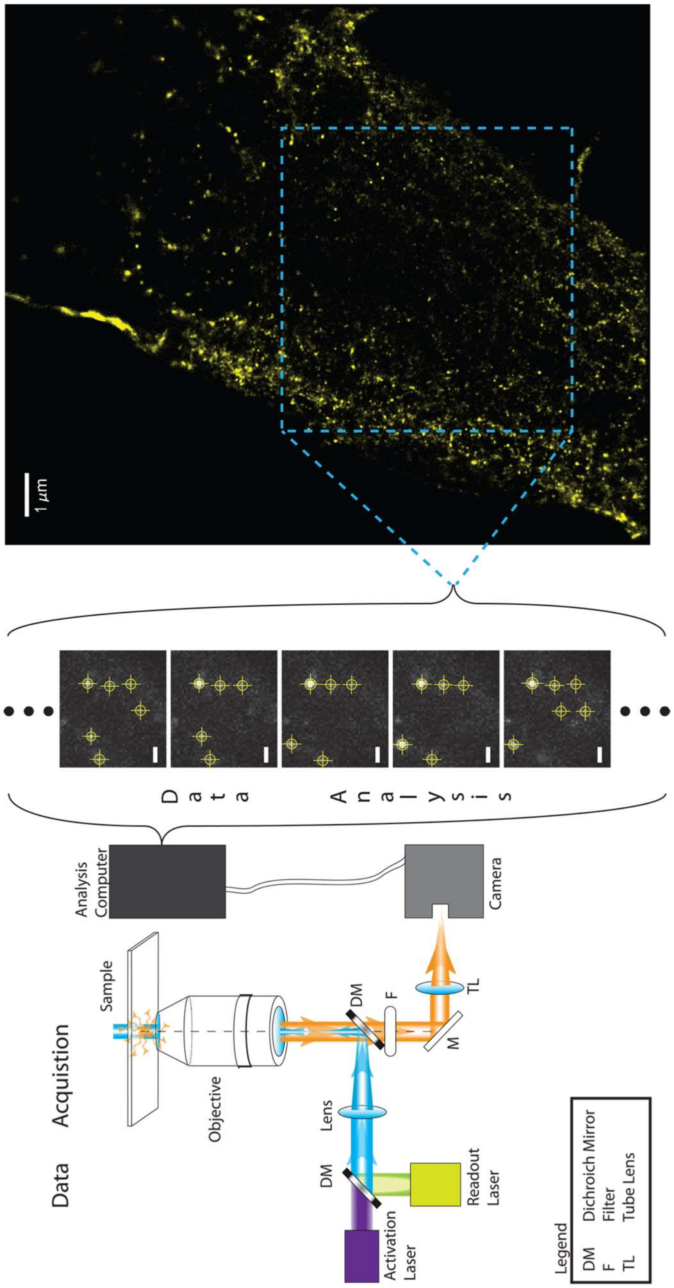
1 μm
Data Analysis
Analysis Computer
Camera
Sample
Data
Acquistion
Objective
DM
F
TL
M
Lens
DM
Readout Laser
Activation Laser
Legend
DM Dichroich Mirror
F Filter
TL Tube Lens

FIGURE 1: This figure shows an essential setup for a single color SRFLM experiment with laser epi-illumination. Two lasers, activation and readout, are made collinear through the addition of a dichroic mirror. The parallel beams then pass through a convex lens that sits at approximately one focal length away from the focal point of the objective in the back aperture. This allows the sample to be illuminated over an area of ~100-1000 μm^2 by nearly parallel laser light. Active molecules illuminated by the readout laser fluoresce until they bleach, and a portion of their emission is captured by the objective lens. Detected fluorescence is separated from other detected light by a dichroic mirror and emission filter. The fluorescence is then imaged by a tube lens onto the sensor of an EMCCD camera. The camera detects the fluorescence, a movie of which is recorded by a computer. The computer localizes each fluorophore by fitting a Gaussian function to the PSF and recording the position of the center of the Gaussian. Coordinates of localized molecules are plotted to form a superresolution image. Scale bars are 1 µm.

until photobleaching irreversibly. This fluorescence is collected by the illuminating objective; laser light is rejected by the dichroic mirror and emission filter(s); the fluorescence is then focused by one or more lenses to form an image on the camera sensor.

The probes emit as a dipole-point source. Thus, when imaged by a lens they appear as a point spread function. Ideally, the point spread function spans several camera pixels, allowing one to fit the image with a PSF(typically approximated with a 2D-Gaussian function), and determine the location of the center of the PSF. It has been shown that fitting a 2-dimensional Gaussian function to the signal provides significantly better localization of the particle than using a center of mass calculation using pixel values [13]. Other fitting algorithms such as Simultaneous Multiple-Emitter Fitting and DAOSTORM can help localize molecules whose point spread functions overlap, increasing the density of molecules that can be imaged on each frame[14, 15]. One disadvantage shared by these fitting algorithms is they do not take into account a fluorophore's ability to blink, which would appear as two independent localizations. Bayesian localization analysis uses Hidden Markov models and Bayesian statistics to reconstruct the probable location of a molecule. This method uses the total number of emitted photons, not just the number of photons on one camera frame, to localize a fluorophore thereby improving the LU. The main drawback of this analysis is the computer power necessary to efficiently process a data set[16].

By controlling the laser intensities one can create an environment where it is uncommon for two probes to fluoresce within a diffraction limited distance *d* of each other. Depending on the intensities used, the probes can be made to photobleach within one or several camera frames. The camera records the emission events of these diffraction limited point sources. By allowing the acquisition to run for multiple camera frames, one can use time to separate the emission of two probes that coexist spatially within a diffraction-limited distance. As shown in figure 1, a computer can fit 2-dimensional Gaussian functions to most of the molecular images acquired by the camera, and can determine their positions, uncertainties, and number of detected photons. After many frames(many localizations), the recorded localizations can be rendered together as a super resolution image [2-4].

1.3. Probes Compatible with SRFLM

Probes for localization microscopy must be controllable(typically with light) such that the majority of probe molecules are within a dark(non-fluorescent) state at any given time. In the case of photoactivatable fluorescent probes, these molecules start off in a dark state which can be activated by light(i.e. the activation laser) into a form that is fluorescent under excitation by the readout beam. Photoswitchable fluorescent probes can be converted by light from one emissive state into another(i.e. from emission of green to red fluorescence). Upon excitation with the switching wavelength, a photoswitchable probe may appear to disappear from one channel and appear in a second one, thus allowing a sparse distribution of probes to be imaged within the second channel. Photoactivation and photoswitching can be reversible or irreversible; reversible activation allows repeated sampling of the same probe molecules over time, but converting the number of localizations into an absolute number of probe molecules is difficult. Irreversibly photoactivatable labels can be more straightforward to count, but timelapse imaging of a given structure over time relies on sampling of different molecules in each subset, which is limited by depletion of the inactive pool of molecules over time.

Fluorescent proteins, caged organic dyes, and conventional organic dyes are the most commonly used fluorescent probes in localization microscopy. Genetically-encoded photoactivatable and photoswitchable fluorescent proteins are very flexible because of the ability to control conjugation to a protein or other biomolecule of interest, expression level over time, subcellular localization, and many other properties accessible to fluorescent proteins in general. PAFPs are ideally suited to live-cell imaging because of their moderate size, relative non-invasiveness and the convenience of labeling cellular structures by transfection. Several recent reviews compare the wide variety of currently available options. The first live-cell localization microscopy used PAFPs [17]. Monomeric forms of PAFPs should be used to minimize self-aggregation [18].

Conventional organic dyes may be used for localization microscopy provided the proper conditions can be obtained such that the majority of fluorophores are within long-lived dark states. Conditions which achieve this requirement have been determined for a large number of such probes, and often require the presence of thiol or other reducing agents within the imaging buffer [19-21]. The small size of organic dyes and the relatively large number of photons they emit make them advantageous for applications where minimization of localization error is desired. However, while organic dyes may be attached to small molecules(e.g. phalloidin) for targeting to specific biological structures, if used for antibody labeling, they must be conjugated to a much larger(i.e. ~10 nm) molecule. This molecule then either binds the biomolecule of interest directly or binds a primary antibody against that biomolecule, which introduces additional localization errors. Since the use of antibodies is typically limited to fixed permeabilized cells or applications where molecules on the cell exterior are labeled, and the introduction of thiol or other reducing agents can affect live-cell physiology, the number of live-cell applications of organic dyes conjugated to antibodies is more limited than those accessible by PAFP labeling. Recently, Shim et al. have demonstrated STORM of conventional fluorophores without BME in the imaging buffer [22], suggesting potential for even larger numbers of applications in live cells. Since localization precision *and* label density are both important for localization microscopy, the accessibility of the antigen within the molecule of interest, the turnover rate(in the case of PAFPs) and potential for problems induced by overexpression are also crucial considerations that can limit the density of labeled molecules and ultimately the image quality. Caged organic dyes are another option for labeling cells, the advantages of which are similar to other organic dyes, but without the requirement for reducing imaging buffers, however many caged dyes do require the use of an activation laser. With respect to both conventional and caged organic dyes, recently developed methods to couple these probes to small genetically-encoded binding sites that can be expressed in cells has enabled live- and fixed-cell labeling schemes that enjoy many of the advantages of both PAFPs and organic dyes [23-28], although these tags can suffer from background [25].

1.4. Advanced SRFLM Methodologies

The super resolution microscope can also be used to measure protein interactions through the implementation of multi-color techniques, and other technological adaptations. It has been shown possible to measure the anisotropy of an imaged molecule allowing for questions about short range order to be investigated[29]. Single particle tracking is also compatible with live cell studies allowing for observations on diffusivity of proteins[30]. Three dimensional localization imaging can have axial localization precision as good as a couple of nanometers[31].

1.4.1. Multiple Channel Imaging

As many biological questions of interest relate to molecular interactions, the ability to image multiple fluorescent probes simultaneously with super-resolution methods has been of immediate interest. Several publications describe schemes for detection of multiple molecular species either sequentially [32-34] or simultaneously [35-39].

Simultaneous detection of multiple species of fluorophore is most often accomplished through the use of a dichroic in the detection path used to direct photons to one channel or another based on their color. In Gunewaredene et al. we describe a multicolor method based on division of the fluorescence into two spatially separate, simultaneous images with distinct wavelength ranges(e.g. the 560-610 nm fluorescence in one and the 610-660 nm fluorescence in the other). The relative intensity of each molecule in the two channels is then used to identify the type of molecule. Images with three PAFPs in living and fixed cells have been demonstrated [36]. As many as four different organic fluorophores have been successfully visualized simultaneously in fixed samples [37].

Sequential measurements take advantage of the photophysics of the fluorophores to separate when fluorescent species emit. In these experiments the goal is to minimize fluorescence from one species, while maximizing the fluorescence from the other species, this can be accomplished in different ways. If the probes' absorption and emission curves are well separated, it is possible to illuminate a sample with one wavelength and record fluorescence from one type of fluorophore, while the second species remains dark. Later a different wavelength can be used to illuminate the sample, and detection filters can be switched to capture the fluorescence from the second species, while the first species remains dark[33]. Alternatively, the fluorescence of a species can be controlled by photoswitching. By using a combination of illumination schemes, illumination with a specific wavelength at a specific frequency, it is possible to sequentially image multiple fluorescent species sequentially[34].

In a dynamic sample, the coordinates of individual molecules obtained over multiple camera frames can be used to construct molecular trajectories, with which diffusion and other kinds of motion can be quantified. While most trajectories obtained in this way will have a limited length(i.e. from a few to a few tens of steps), the number of molecules sampled and hence the total number of trajectories can be very large(tens of thousands or more). The same trajectories can be used to map molecular mobility, chart cluster boundaries, and quantify confinement at the nanoscale [30].

In 2008 it was demonstrated that a researcher could measure the anisotropy of a fluorescent probe relative to other fluorescent probes, while collecting spatial information, by the introduction of a polarizing beam splitter into the fluorescence detection path. The polarizing beam splitter separates the fluorescence signal into two orthogonally polarized images on the camera chip with intensities $I_{\parallel}$ and $I_{\perp}$. The two images can be mathematically overlaid onto each other, and the fluorescent probes can be localized in space. The signals in the separate channels allows a measurement of the probe's intensities $I_{\parallel}$ and $I_{\perp}$, from which the probe's anisotropy, r, can be calculated as follows.

$$r = \frac{I_{\parallel} - I_{\perp}}{I_{\parallel} + 2I_{\perp}} \qquad 2$$

If probes are able to rotate while attached to the molecule of interest, then the measured anisotropy will reflect a time-average of the orientation of the probe. This technique has been used to visualize trends in probe orientation in biological samples and is compatible with live cell imaging [29].

1.4.2. Three-Dimensional Imaging

Superresolution localization microscopy is also capable of sub-diffraction limit resolution in the axial direction through the use of a few techniques, namely astigmatism imaging, biplane imaging, and interference-PALM or iPALM. It is natural to talk about astigmatism imaging and biplane imaging together as they both take advantage of the predictable distortion of the PSF as imaged between two focal planes. In astigmatism imaging, a long-focal-length cylindrical lens is placed in the optical path way spatially separating out the focal point for the x and y directions along the path of the signal towards the camera. The camera is placed at approximately half way between the two focal points and data is then collected. As the probe emits above or below the median focal plane its PSF will be focused in one of two orthogonal directions, by measuring the ellipticity of the PSF, the axial coordinate can be determined to as within as 60 nm error [40].

The biplane method utilizes a beam splitter to create to detection pathways of differing length. The point spread function will then have different representations between the two pathways. If the distortion in the PSF between the two focal planes is known, which can be determined through the use of fluorescent beads, then fitting algorithms can measure the center of the PSF, which gives the lateral coordinates. The PSF can also be analyzed to find the degree of distortion if it sits near or far from one of the two planes, by measuring the degree of distortion of the PSF it is possible to measure the axial coordinate of the localization with error of up to 75 nm [41].

iPALM takes advantage of the quantum nature of photons to make axial measurements. The geometry of the iPALM microscope is similar to that of a 4Pi microscope. The iPALM uses two objectives focused to a common plane in the sample, and then combines light from the two paths through a series of beam splitters, then onto three separate cameras. The quantum nature of the photon will give rise to interference effects based on difference in axial path length between the two objectives; the axial position is determined by the relative intensities of the molecule within the images obtained by the three cameras. The axial coordinate of fluorophores can be determined with localization errors of less than 4 nm [31].

Dual-objective STORM added a second objective to the astigmatism setup to increase the number of collected photons per localization. Since localization uncertainty goes as $1/\sqrt{N}$, adding a second objective can decrease localization uncertainty by almost a factor of 0.7 from what it would be with a single objective. The two objectives are focused to the same focal plane, but send the collected fluorescence to different cameras. The two cameras can be focused to a common focal plane, or they can be focused to different focal planes, thus combining the biplane approach into this technique as well[42].

Three dimensional coordinates can also be obtained by using the double helix point spread function(DH-PSF), instead of the classical point spread function. The DH-PSF is created by modulating the Fourier transform of the PSF through the use of a spatial light modulator(SLM). The resulting image consists of two lobes whose orientation gives axial position, and whose midpoint gives lateral coordinates of the generating molecule. Localization uncertainties have been demonstrated to be ~10-20 nm[43].

1.5. Spatial Resolution

In SRFLM, several factors are crucial in determination of image quality and spatial resolution. For example, the labeling density, localization precision, degree of sample drift correction, and integrity of the sample during imaging must be considered when designing a super resolution experiment.

Localization uncertainty(LU) is another important factor in determining resolution. LU measures the uncertainty in the determination of the location of the molecule from its image. As discussed previously, LU depends in part on the background noise, photons detected, pixel size, and the profile of the diffraction-limited PSF. Pixel size can be altered by adjusting the total(optical) lateral magnification of the microscope system; the effective size of image pixels should be large enough so the PSF spreads over multiple pixels. Reduced magnification(large pixels) increases LU, but increasing magnification reduces the number of photons per pixel, which makes molecules harder to detect against background. A larger number of photons detected typically results in smaller LU. With enough photons detected, and careful experimental setup, the background noise contribution to the LU can be made small compared to other sources of error. A significant contribution to poor LU is the radius of the PSF. In an experimental system, the distribution of molecular orientations, optical aberrations, molecular motion, and sample drift can distort or blur the PSF and increase localization errors, leading to degraded resolution.

Label density plays a substantial role in the effective resolution of a rendered SRFLM image. The Nyquist-Shannon sampling theorem claims that in order to fully reconstruct a periodic signal of frequency f it should be sampled at a minimum of $2f$. Applying this to the idea of imaging if we measure a spatial density of ρ, the Nyquist resolution would be $1/\rho^{\frac{1}{D}}$ where D is the dimensionality of the image. However, recent studies have introduced an effective measure of resolution which combines the effects of localization and density, without requirement for periodic samples or use of the Nyquist-Shannon theorem [44]. This important work also shows that using either LU or Nyquist resolution estimates alone can often overestimate the true spatial resolution present in an image.

1.6. Optimization of Image Acquisition

Sample drift can degrade the quality of an image. If the drift is large over the exposure time of a single frame, then the PSF of a molecule can be distorted giving a bad fit, and thus lower localization precision. If the drift is significant enough over a data set, then the reconstructed image will have a blur, similar to slowly panning a camera while taking a long exposure image. This latter problem can be addressed either while taking data, or after the measurement has been performed. Through the use of active monitoring and a computer controlled microscope stage, the drift can be corrected by a computer in real time by observing the position of a fiducial. Such methods can reduce drifts down to below 0.1 pixels over timescales of hours [45]. Another method, applicable only to fixed samples, is to mathematically reduce the drift after the data has been taken using autocorrelation [46].

Because fluorophores emit as optical dipoles, the image of a fluorophore has a strong dependence on angle and proximity to the focal plane. Significant and systematic localization errors can arise as a result of the dipole orientation of individual molecules imaged with high NA lenses; inaccuracies as large as 10-20 nm can result when using 1.4 NA objectives to image individual fluorophores. Use of 1.2 NA objectives reduces collection efficiency but in many cases reduces the magnitude of position errors to <10 nm [13]. Experiments have shown that for fixed probes, the uncorrected localization error due to probe orientation can be as great as 200 nm. This error was shown to be dependent on the axial position of the molecule, as well as the orientation of the probe. These effects were circumvented by using the double-helix PSF imaging method[47].

Illumination of biological samples with high-intensity light can cause photodamage; thus, it is essential to be mindful of the laser intensities used in a localization experiment, especially for live-cell studies. Especially in high speed imaging where peak readout intensities can reach as high as 15 kW/cm^2, precautions should be taken to minimize cell exposure to this intense radiation. Using a TIRF geometry will help limit the amount of sample volume exposed to the radiation, and by limiting imaging time to a few seconds, photodamage can be mitigated to some degree.

1.7. Live-Cell Compatibility

When studying biological order, fixed cell studies can offer important information about structure, but falls short when trying to uncover dynamical processes. The ability to capture the dynamics of an active system allows researchers to answer more questions about interactions. Shortly after the announcement papers, FPALM was demonstrated to be compatible with living samples [17]. This development has allowed researchers to investigate biological dynamics on unprecedented length scales. SRFLM can be built from a conventional fluorescent microscope, and is compatible with many microscope stages and stage incubators(i.e. for use in imaging living samples). As with the CLSM, precautions must be taken to ensure sample integrity when deciding laser exposure time and laser intensity at the sample.

1.8. Going Faster : Improving Temporal Resolution

The amount of time required to capture an image is partially determined by the desired spatial resolution of the final image. For the highest possible spatial resolution, high localization density is required, which requires localization of many subsets of molecules and therefore acquisition of many camera frames.

The rule of thumb is that the number of localizations within the structure of interest on the length scale of interest should be much larger than one; for example if a structure is to be imaged on 50 nm length scales, then within this structure there should be a density of localized molecules much larger than one per 50 nm x 50 nm area. In order to localize enough molecules to satisfy this constraint, while keeping the molecules within each frame well separated from one another, the number of camera frames will need to be much larger than approximately the square of the ratio of the diffraction-limited PSF width(i.e. ~250 nm) divided by the length scale of interest(i.e. 50 nm), so at least$(250/50)^2 = 5^2 = 25$. Thus, 100 camera frames would yield at best ~4 molecules localized per 50 nm x 50 nm pixel. Furthermore, molecules visible for more than one successive frame prevent others from being imaged and may also limit time resolution. On the other hand, use of multi-emitter fitting algorithms has recently offered a new option which can provide both high density of localization and improved time resolution; more molecules can be localized per frame, proportionately reducing the total number of frames required to obtain good sampling of a structure [16].

Fluorophore properties are one limitation to acquisition rate, since they have finite emission rates at saturation, and thus it takes some amount of time(e.g. 10^{-4} to 10^{-3} seconds) to squeeze all the photons out; the high laser intensities needed to induce the maximum emission rate per molecule can also damage cells.

To acquire many camera frames requires more time, or faster frame rates. Frame rates are to some degree limited by the camera technology: sCMOS cameras can image in excess of 1000 frames per second, while CCDs are often slower [5]. Usually the increased frame rates require a smaller region of interest be measured. This limitation comes from the speed at which the camera pixels can be read out. To achieve frame exposure times necessary for high temporal resolution(sub second per rendered image) frame rates of > 500 Hz(<2 ms exposure time) must be used. To achieve these speeds many cameras reduce the number of pixels that are active during imaging. By reducing the pixel area on the camera chip the frame exposure time can be decreased down to <2 ms. This decreased effective camera chip size requires a small region of interest to be imaged(e.g. 5-10 μm in diameter), but since nanoscale details are often of interest in such experiments, an ROI of 5-10 μm is sufficient for many applications. Use of sCMOS cameras has enabled acquisitions of live-cell SRFLM images at video rate [5].

1.9. Future Directions

Localization microscopy(SRFLM) has broken the diffraction limit for fluorescence microscopy, and now routinely provides resolution in the tens of nanometers in living and fixed cells. Advancement of the capabilities could come from improved fluorescent probes emitting larger total numbers of photons at higher peak rates, improved instrumentation to correct for various sources of localization errors and inaccuracies, from faster low-noise cameras with high detection efficiency, and from improvements in localization algorithms, particularly those allowing multiple emitters to be localized at short range, or those that can better discriminate between emitters and noise. Perhaps the most important question, though, is which biological problems are best suited to these methods to allow important discoveries to be made.

In future chapters, we will investigate some of the challenges involved with imaging at higher temporal resolutions using fluorescent proteins. Pushing the temporal resolution is necessary to better understand how many dynamical systems in biology operate. As we push the temporal resolution higher we notice that the spatial resolution of the final render begins to suffer. The main problems we face are those of higher background, lower fluorescent signal, and under sampling of structures from fewer localized molecules. If we are to investigate some dynamic biological systems below the diffraction limit, it is critical to understand and overcome the problems that arise with imaging at higher speeds.

The next chapter looks at how experimental design can be used to reduce background in some biological systems, and investigates potential issues arising from fewer localizations in final renders. We show that it is possible to find molecules with frame exposure times as low as 1.45 ms and render times of 0.1 s. We also use computer simulation to address questions of under sampling biological of structures. The final chapter investigates a new algorithm for detecting molecules in localized data. We show that this algorithm has strong success regardless of the pattern produced by the PSF(regular or astigmatic). A robust identification algorithm can allow for more reliable detection of molecules in noisy data, which is common in high speed imaging. Additionally a generalizable identification algorithm could potentially be used for different localization methods, such as multi-emitter fitting[15] which can allow for improved sampling with a given temporal resolution, or improved temporal resolution with a given level of sampling. These two chapters describe and quantify some of the problems associated with high speed localization microscopy, and present possible mechanisms of overcoming some of these problems.

CHAPTER 2

HIGH SPEED FLUORESCENCE PHOTOACTIVATION LOCALIZATION MICROSCOPY IMAGING

The following chapter is reproduced from parts of the published conference proceedings by Nelson *et. al* 2014[1].

Imaging live biological samples to study biomolecular dynamics requires a very high spatial and temporal resolution. Superresolution localization microscopy has allowed researchers to investigate biological systems whose sizes are below the diffraction limit(200-250 nm) using an optical microscope. Fluorescence Photoactivation Localization Microscopy(FPALM) and other localization microscopy techniques have recently been shown to be capable of rendering superresolution images obtained with acquisitions of shorter than 0.5 seconds. Here we will discuss the FPALM imaging technique, at both lower and higher imaging speeds. This chapter will focus on the advantages, challenges, and drawbacks of high speed imaging localization microscopy.

2.1. Results

We present detection of multiple fluorescent proteins in sufficient numbers to allow rendering of a superresolution image within a fraction of a second, without the use of multi-emitter fitting. In turn this has allowed for the development of a new technique named "Fast FPALM" which is capable rendering superresolution images on time scales of ~0.1s. This technique is demonstrated with two fluorescent proteins, Dendra2 and PAmCherry. The technique was performed with a typical FPALM illumination geometry, sometimes implementing total internal fluorescence(TIRF) microscopy alignments to decrease background noise. Our detection path used either a Hamamatsu Orca Flash 4.0 sCMOS camera or an iXon series EMCCD.

Using the iXon camera isolated crop mode, we were able to image live NIH3T3 cells expressing Dendra2-Hemagglutinin(Dendra2-HA) with a standard inverted fluorescence microscope(Olympus IX71). HA is an influenza virus membrane protein that allows the virus to attach to host cell, and eventually mediate the formation of a membrane fusion pore. The ability of HA to perform its biological function is dependent on its clustering within the viral membrane.[48] Cells were selected by viewing the pre-activation fluorescence(its green form) of Dendra2 illuminated with a mercury lamp. The cell membrane was brought into the focal plane by increasing the frame exposure time to 10 ms, while illuminating the sample with ~4 kW/cm^2 excitation light in a TIRF geometry. Once the sample was focused, the illumination was turned off. High speed imaging was done using ~15 kW/cm^2 peak excitation and ~5 W/cm^2 peak activation intensities while the camera recorded 690 frames per second. The resulting data set was analyzed and 0.1s(or 0.5s) renders were created from 69(345) sequential frames, respectively.

Simulations were used to compare the dynamics observed in the HA clusters to the fluctuations that would be expected from repeatedly undersampling the same structure. For the simulation, stationary(non-dynamic) clusters were defined as filled, spatially fixed circular shapes with perimeters and areas matching those of the measured set. Several collections of points were selected from inside the cluster, and were given an arbitrary displacement in x and y chosen from a normal distribution with a mean of zero and a standard deviation equal to the localization uncertainty measured from fixed cell data. The number of points in each set was chosen at random from a normal distribution centered at the average number of molecules detected per cluster, and with variance equal to that of the measured cluster set. The structure was repeatedly sampled until the average and variance of the perimeter and area did not change noticeably with successive sampling. Simulation results showed a standard deviation in areas equal to ±0.010 µm^2 and in perimeter equal to ±0.098 µm. Cluster analysis reports a standard deviation of ±0.020 µm^2 and ±0.166 µm for area and perimeter respectively of an HA cluster repeatedly sampled at 1/10 s intervals in a live sample.

To image at frame rates above 700 Hz, the sCMOS camera was used in place of the EMCCD. Using a chip area of 100x100 pixels we were able to achieve a frame rate of 1026 Hz(exposure time of 0.975ms). We imaged NIH3T3 cells expressing either Dendra2-HA or PAmCherry-Cofilin. Cofilin is a cytosolic actin binding protein that has been found inside purified influenza virions.[49] The interaction of cofilin with influenza viral proteins is currently under investigation. Cells expressing Dendra2-HA were found as described previously, while cells expressing PAmCherry-Cofilin were found by illuminating with ~4kW/cm^2 intensity excitation light until a cell emitted a deep red fluorescence. Molecules were brought into focus in the same way as described above. Similar intensities, as previously described, were used to image the molecules at high speed. The sample was exposed to laser radiation for 1 second, which was controlled by a mechanical shutter triggered by the camera. At this frame rate, we could still resolve Dendra2 and PAmCherry molecules, while detecting less than 100 photons on average per frame per molecule.

FIGURE 2 Typical High Speed FPALM Results

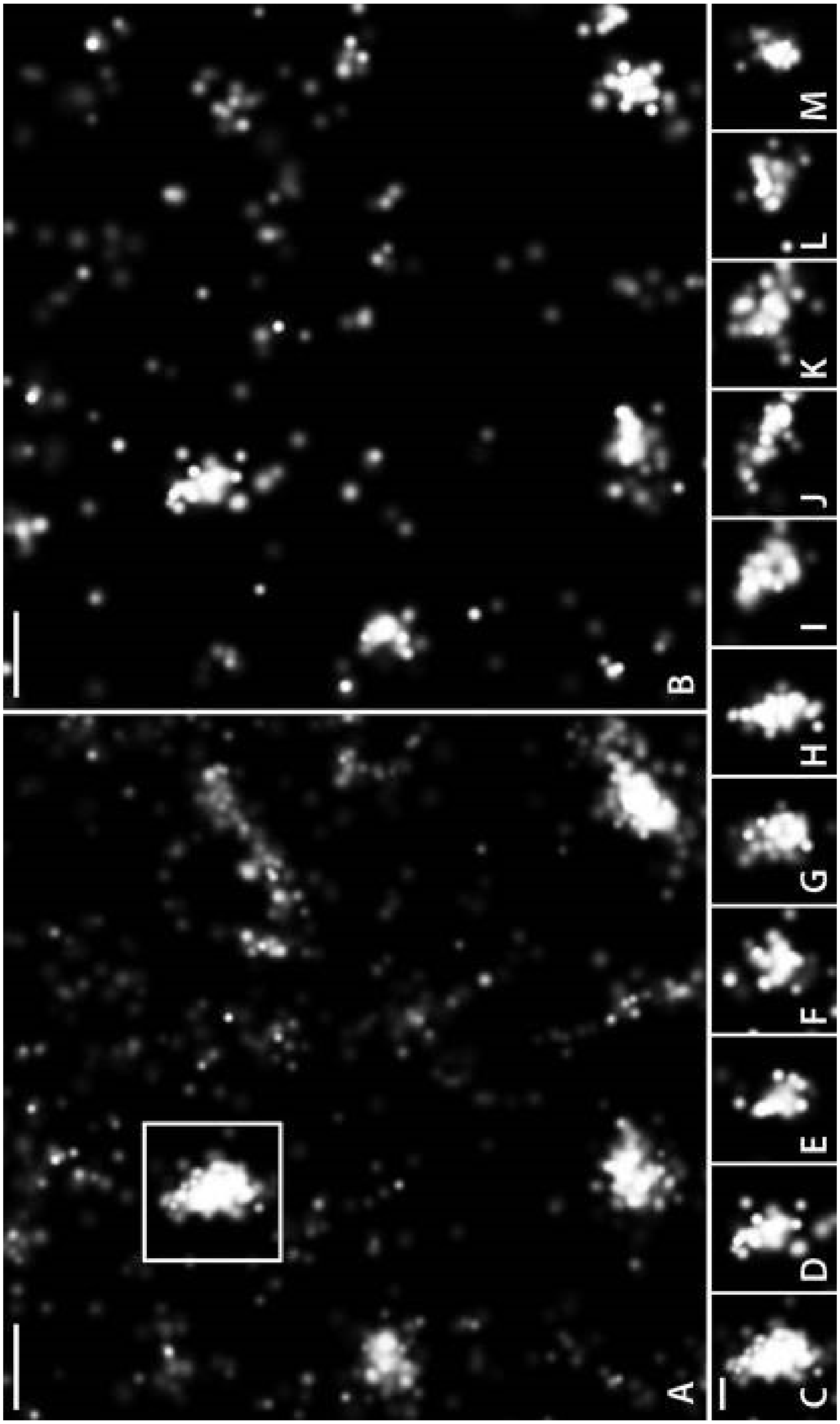

FIGURE 2: A) 0.5 s FPALM render of a live NIH3T3 cell expressing Dendra2-HA. B) 0.1 s FPALM render of the same cell in A. C) Enlarged image of the area within the red square in (A). D-M) Consecutive 0.1 s renders of the same area over a full second. Scale bars are as follows A and B: 500 nm, C-M: 200 nm.

2.2. Discussion

2.2.1. Cluster Dynamics

As Figure 2 demonstrates, the HA clusters are dynamic on time scales as short as 0.1s. Due to the limited number of molecules localized in the final image, simulations have to be performed to ensure that the dynamics observed are representative of the behavior of the proteins in the membrane, and not due to repeated under sampling of the structure. Our simulations showed a nearly 2 fold lower standard deviation in area and perimeter as compared to the live cell results, suggesting that the fluctuations seen in the HA clusters on these time scales are in fact representative of the clusters behavior, and are not due to undersampling.

2.2.2. Limited Number of Detected Photons per Molecule per Frame

One of the primary issues in high speed imaging with FPs is the limited number of detected photons(N) within the short time per frame. Because localization uncertainty scales as $1/\sqrt{N}$, the localization precision is degraded significantly by low numbers of detected photons per frame[7]. This problem can be highly exacerbated, for example, if the excitation rate of the molecules is suboptimal for the given frame exposure time. Thus, to enable detection of probe molecules, it is crucial to match the photobleaching time of the probe molecules to be approximately equal to the frame exposure time.

However, the problem of small N is not entirely mitigated by carefully selecting the desired excitation rate for imaging. Typically a high excitation rate of the fluorophores is achieved by using intensities of the excitation source higher than what is typically used in superresolution experiments(~15 kW/cm^2)[5, 23]. Some fluorescent proteins have been observed to emit fewer photons(before bleaching) at higher intensities, including mEos2 and tdEos[23]. There exists evidence to suggest that these proteins also have an optimum excitation intensity which corresponds to the highest number of photons emitted per second[50]. This effect limits the maximum frame rate when imaging a given FP with a given average N per frame, which will limit how quickly a full superresolution image can be rendered when using a given fluorophore to achieve a given density of localizations.

The limited N at high frame rates causes both localization precision and single molecule identification to become more challenging, especially in the presence of fluorescence background. Improved photon detection strategies such as the 4Pi geometry[51] could help improve the quality of rendered images obtained with small N per fluorophore per frame, as could more efficient detectors and filters. It is possible to add antioxidants to extend the lifetime of the fluorophores, thus increasing total number of photons emitted, but these compounds have not been systematically investigated in the context of photoactivatable FPs, and their effects on cell physiology could potentially complicate interpretation of results obtained in living biological samples.

2.2.3. Fluorescence Background

Fluorescence from outside the focal plane(either out of focus molecules or cellular autofluorescence) contributes to the background, which increases the position uncertainty of localized molecules[7]. The intensity of the background is then related to the number of out of focus molecules being activated and excited. In Fast FPALM this can present a challenge since the signal is typically already weaker than in the slower imaging regime. It is therefore ideal to try to minimize the out of focus fluorescence as much as possible. Fortunately, many previously described methods to reduce the background are compatible with Fast FPALM and other forms of high speed localization microscopy(HSLM). For example, total internal reflection fluorescence(TIRF) excitation has been used with great success[23]. The TIRF alignment creates an evanescent wave with $1/e^2$ penetration depth of usually less than 200 nm, which is suitable for membrane studies, but is too shallow to study many processes that happen deeper in the sample. Other alignment techniques such as highly inclined and laminated optical sheet microscopy[52], variable-angle epifluorescence microscopy[53], or selective plane illumination microscopy[54] can reduce illumination of out-of-focus molecules that would contribute to the background signal. It should be noted that while background reduction techniques are useful and help improve localization uncertainty, it is possible to detect and localize molecules with wide-field illumination, even in cells with modest levels of background and out-of-focus fluorescence, at the cost of somewhat increased localization uncertainty and a higher frequency of missed localizations. This allows researchers to probe processes and interactions that occur deeper into the sample.

2.2.4. Live-Cell Viability

One of the main attractions of high speed imaging is the ability to capture and characterize dynamic processes. As such, in most HSLM experiments the sample will be living, which requires extra consideration. One of the primary concerns is that the excitation intensity in HSLM can be quite high(~10-30 kW/cm^2). In comparison, in a point-scanning confocal microscope, with a 561 nm laser with 100 µW power at the sample, focused by a 1.2 NA objective lens to a diffraction-limited spot with FWHM ~ 0.257 µm, the intensity will be approximately 48 kW/cm^2. Thus, while intensities used in HSLM are high, they are comparable to those used in confocal microscopy, except that in HSLM the entire sample is illuminated at once. Therefore, in addition to considering intensity, HSLM users may want to consider the total dose of electromagnetic radiation absorbed by the sample. By using a shutter and illuminating the sample for the minimum time necessary, it is possible to minimize the total dose of(laser) energy a cell receives during imaging. This can be used to obtain a snapshot of the cell during a short time window while lowering photodamage. However, there is no substitute for proper controls, as sensitivity of biological processes to photodamage will depend on the details of each biological specimen and the methods used to image it. Here, we observed no evidence of light-induced cytotoxicity as assayed using the Live/Dead Viability/Cytotoxicity Kit for mammalian cells(Life Technologies, Carlsbad, CA)(data not shown).

2.2.5. Proper Sampling

To create the shortest possible render, one must localize the smallest number of molecules necessary to properly reconstruct the system at the length scale of interest. This will lower the average nearest neighbor distance, which is one measure of Nyquist resolution[55]. However the structures comprised of imaged molecules do not necessarily form continuous structures and using the Nyquist criterion for resolution may not always be appropriate, as other resolution estimates show[44, 56, 57]. It is also important not to localize too few molecules when constructing a render. If structures are undersampled they can be misrepresented in the render. The undersampling problem can best be exemplified in probing the fast dynamics of a biological structure. Consider a static structure labeled with fluorescent tags imaged over the course of a second. The data set could be divided into 20 subsets representing 50 ms of acquisition time each. If the structure in question is undersampled, then its representation between renders will appear to change due to the random sampling of the molecules between renders. This will cause fluctuations in shape, perimeter, and area of the measured structure, which would not represent actual dynamics. Depending on the degree of undersampling, it is possible for the structure to not appear within some renders, giving the impression that it disappeared and reappeared on very short time scales. To answer whether or not a given system is being undersampled, simulations can provide an indication as to whether the dynamics shown in a data set are a function of live cell dynamics, or undersampling.

CHAPTER 3

MOLECULAR IMAGING WITH NEURAL TRAINING OF IDENTIFICATION ALGORITHM (MINuTIA)

Superresolution localization microscopy strongly relies on robust identification algorithms for accurate reconstruction of the biological systems it is used to measure. The fields of machine learning and computer vision have provided promising solutions for automated object identification, but usually rely on well represented training sets to learn object features. However, using a static training set can result in the learned identification algorithm making mistakes on data that is not well represented by the training set. Here we present a method for training an artificial neural network without providing a training set in advance. This method uses the data to be analyzed, and the fitting algorithm to train an artificial neural network tailored to that data set. We show that the same artificial neural network can learn to identify at least two types of molecular emissions: the regular point spread functions, and the astigmatism point spread function. Simulations indicate that this method can be extremely reliable in extracting molecular emission signatures. Additionally, we implemented the artificial neural network calculation to be performed on a graphics processing unit(GPU) for massively parallelized calculation which drastically reduces the time required for the identification process. By implementing the neural identification on a GPU, we allow this method of identification to be used in a real time analysis algorithm.

3.1. Introduction

FPALM, PALM, STORM, and other superresolution localization microscopy(SRLM) techniques have helped further our understanding of biology by offering researchers a way to directly watch dynamics at length scales below the optical diffraction limit(200-250nm) (See also Chapter 1)[2, 58, 59]. A key step in the processing of the data for these methods is identifying regions in images that contain fluorescent molecular emissions for subsequent localization. While a multitude of algorithms currently exist to perform this function, usually in tandem with subsequent localization, almost all of these methods rely on some previous knowledge of the data set, and the expected result of molecular emission, to help find the molecules[60-64]. Furthermore, many of these techniques are not easily generalizable to methods which augment the conventional point spread function(PSF), such as astigmatism, biplane, or double helix PSF imaging. Building an algorithm that can be easily generalized to multiple imaging regimes or methods could allow for a more streamlined flow of data analytics in SRLM experiments.

The field of data science, specifically machine learning and computer vision, may offer insight into this goal. It was shown that multi-layered feedforward neural networks are capable of approximating any function[65]. A classic example of the power of these artificial neural networks is an algorithm capable of recognizing numerical digits after learning from a training set[66]. Using a basic artificial neural network and a custom feedback learning algorithm, we were able to teach a computer how to identify molecules with the only prior information used being the chosen localization algorithm.

Here we present Molecular Imaging with Neural Training of Identification Algorithm(MINuTIA). This method iteratively trains an artificial neural network on raw data. By basing the success of an identification on how well it was fitted by the localization algorithm, we are able to generate a training set from a subset of raw data frames. This method has the advantage of automatically selecting against biases that would arise from a user created training set. Additionally, as imaging conditions change from experiment to experiment, this method offers the researcher a way for a tailored identification algorithm despite differences in point spread function shape that would arise from different imaging conditions.

While there is a significant increase in calculation time when compared to some other methods, the neural network identification step was written using CUDA software and is utilized as a parallelized image filter whose calculation is carried out on a mid-range graphics processing unit(GPU). This allows for a massive increase in processing speed which ultimately allows for higher data throughput when compared to simpler serial based methods.

3.2. Methods

We designed an ANN capable of discerning molecular emission images for segmentation and subsequent localization. The implementation of this ANN to the identification problem is essentially one of data classification. Specifically, we attempted to differentiate patterns on 49 pixels into those that contained the signature of molecular emissions, from those that did not. As we attempted to do this mathematically, the problem is analogous to a 2-dimensional problem of determining a linear boundary which separates 2 distinct classes of data.

We decided to train the weighting parameters used by the ANN by implementing the back-propagation algorithm[67] on training data. Initially we used supervised learning techniques by selecting images from experimental data as well as computer generated approximations of molecular emission images. We noticed that the resulting ANN would consistently pick out image regions that resulted in poor localization fits. We realized this was a problem with the images used to train the algorithm and changed our method to an unsupervised learning technique.

The process starts by randomly assigning values to all node weights in the ANN. This randomization helps to break any symmetry artifacts that could arise in the neural network training if all ANN parameters were initialized to the same value. If multiple data sets are being used to train the ANN, first a random data set is chosen, then random frames from the dataset are chosen to be analyzed. The decision was made in an attempt to prevent the training from biasing the final neural net towards any particular data set, or particular frame. The raw frames are preprocessed by using rolling ball subtraction to remove some background from the images[68]. The randomized ANN then analyzes every pixel from the background subtracted frames to determine if a molecule is contained in the region surrounding a central pixel. The "identified" areas are segmented and fed into a localization algorithm. Here we used Maximum Likelihood Estimation(MLE) to fit a Gaussian approximation. The results of the fit are then analyzed and subjected to a tolerancing function. This step decides whether an identified region results in a good or poor fit based on user selected tolerances of the fitting parameters and reported errors from the MLE fit.

To help speed the learning process, if an insufficient number of well-fitted regions are identified on the first iteration, a new neural net is generated as described above and new regions are identified and tested. All the regions identified are held in memory. When a sufficient number of positive regions have been found, this step terminates, and the algorithm trains the neural network based on the training set. Without this step, MINuTIA is susceptible to only learning from a collection of negative images, which prevents any subsequent identification of positive regions, and requires the user to restart the process.

FIGURE 3 Example of Learning Process

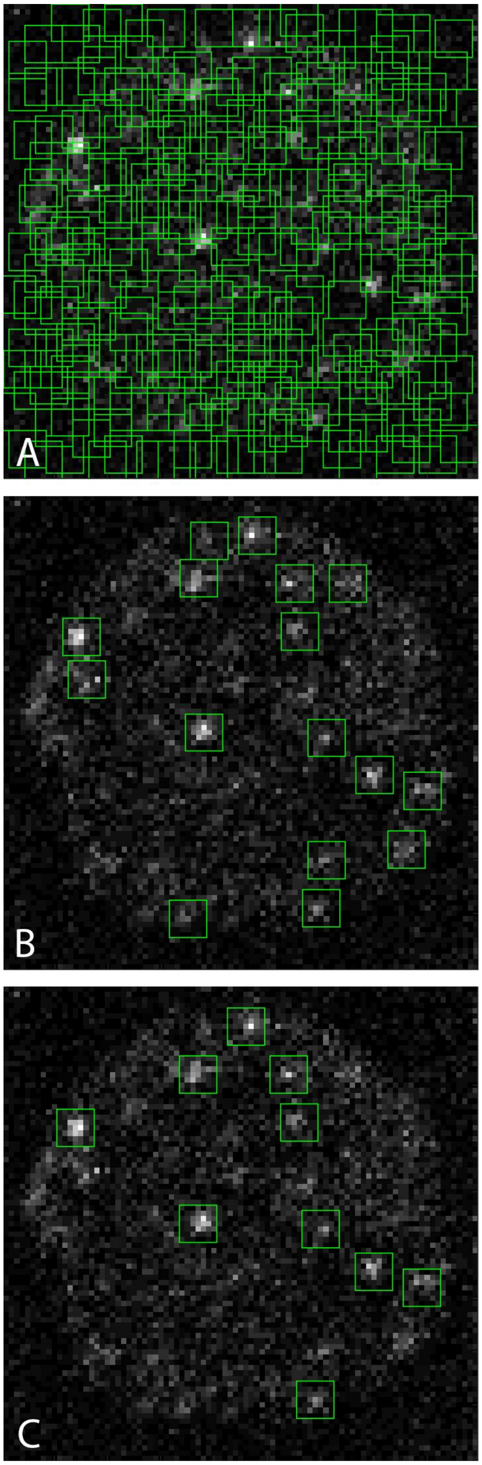

FIGURE 3: The results of the training process are shown above. A) Shows the identifications that result from the untrained neural net. B) Identification result after a single training session. C) Identification result after many training sessions. Here it is shown the increasingly preferential nature of the neural network to pick out regions that will result in a strong fit with the localization function.

The learning algorithm then saves all segmented images and creates an 'answer key' consisting of a value of 1 or 0 depending on whether the image(subregion) resulted in a good or poor fit respectively. The segmented images and answer key are used to train the weighting parameters of the ANN by minimizing the following logarithmic cost function.

$$C = \left(\frac{1}{m}\right)\sum_{i=1}^{m} y_i * \ln(a_i) + (1 - y_i) * \ln(1 - a_i) + \frac{\lambda}{2m} * \sum_{j=1}^{n} \Theta_j^2 \tag{3}$$

Where C is the final cost, m is the number of training sets, y_i is the desired determination of training set i, a_i is the obtained result using current fitting parameters represented by Θ, λ is an overfitting parameter. The second sum acts to penalize the cost when more fitting parameters are used.

The process then repeats. Each iteration adds to the total number of training images. This helps prevent the ANN from repeating mistakes that could occur from removing older images. In the interest of computer memory we removed a random 5% of the positively identified images. This prevented the process from repeating mistakes by removing from the negatively identified images, and makes the process less susceptible to falsely identified positive results. The program is allowed to continue using a new data set and a new list of frames until the ANN identifies successfully fitted image regions at a user determined rate, or until terminated by the user.

We noticed that during the early iterations, the parameters were not optimized enough for high specificity in region selection. This caused a large number of regions to be identified for fitting and subsequent training. To help speed up the learning process we limited the number of frames analyzed in the early iterations to only 10 frames of a data set; after the 15th iteration, this number was increased to 1000 frames from a dataset.

The ANN was organized in a single layered feed forward architecture[65] comprised of an input layer, single hidden layer, and output layer as represented in figure 4. The input layer consists of a linearized array of pixel values which comprise the nxn pixel region. The activation function for each node in the hidden layer and output layer was chosen to be the Sigmoid function[69].The final value of the central pixel of an n by n pixel image is calculated using the following equations.

$$Z_m = \sum_{i=0}^{n^2} \Theta_{mi} * P_i \tag{4}$$

$$a_m = (1 + e^{-z_m})^{-1} \tag{5}$$

$$Z_{out} = \sum_{j=0}^{m} \Theta_j * a_j \tag{6}$$

$$a_{out} = (1 + e^{-z_{out}})^{-1} \tag{7}$$

Where P_i is the pixel value of the ith pixel, Θ_{mi} and Θ_{out} are the learned parameters linking the ith pixel to the mth neural node, and the m +1 neural nodes to the output node respectively, Z_m and Z_{out} are the arguments to the sigmoid function for the mth neural node and the output node respectively, a_m and a_{out} are the activation values of the neural nodes, $a_{out}$is the final value output by the neural network. All sums start at the 0 index to incorporate the bias unit needed for proper calculation[70].

As with most classification and fitting problems, one must determine the optimal number of parameters for use in the fit. Too few parameters result in poor classifications and too many can result in overfitting(and inefficiency). In the case of ANNs this choice of parameters is encoded in the number of neural nodes used. We trained ANNs with different numbers of hidden layer nodes to check for underfitting by looking as how well the neural net identified known images. Our training set was divided randomly into a 70 - 30 split where the ANN was trained on 70% of known images and then tested on the remaining 30%. In artificial neural networks, overfitting occurs when the network has memorized the test set; as such, using a neural network with 30 hidden layer nodes would not be susceptible to overfitting if presented with an order of magnitude more test images as was the case here. Instead, increasing the number of nodes would allow the neural network to better identify regions[65] at the expense of computational cost. As such we ran simulations to find that using more than 30 hidden layer nodes did not greatly affect the performance of the neural network(Figure 5).

Each of the pixel values being analyzed is sent to each of the 30 nodes with different weighting parameters. An activation value is calculated for each node which is then sent to the output node. The output node computes the final activation value for the area by again combining the inputs with respective weighting values and computing an activation value that lies between 0 and 1. The decision to segment and localize is made if the output value is above 0. The cutoff of 0.5 is chosen because this is the resulting value of the sigmoid function when the argument is 0. To prevent over counting of a region that has multiple pixels with activation values above 0.5, we add the requirement that the activation value of a pixel must also be the maximal value in a 5 pixel by 5 pixel neighborhood.

The ANN analyzes data around a central pixel to determine an activation value for that pixel. For our implementation we used a 7 pixel by 7 pixel window, but this size can be scaled to accommodate any imaging modality. The activation value represents a measure of certainty that the surrounding region will result in a good fit. The activation value of one pixel is independent of the activation value of any other pixel as the activation values do not depend on each other. This has the advantage of making the problem of measuring an activation value of all pixels

FIGURE 4 Example of Artificial Neural Network Architecture

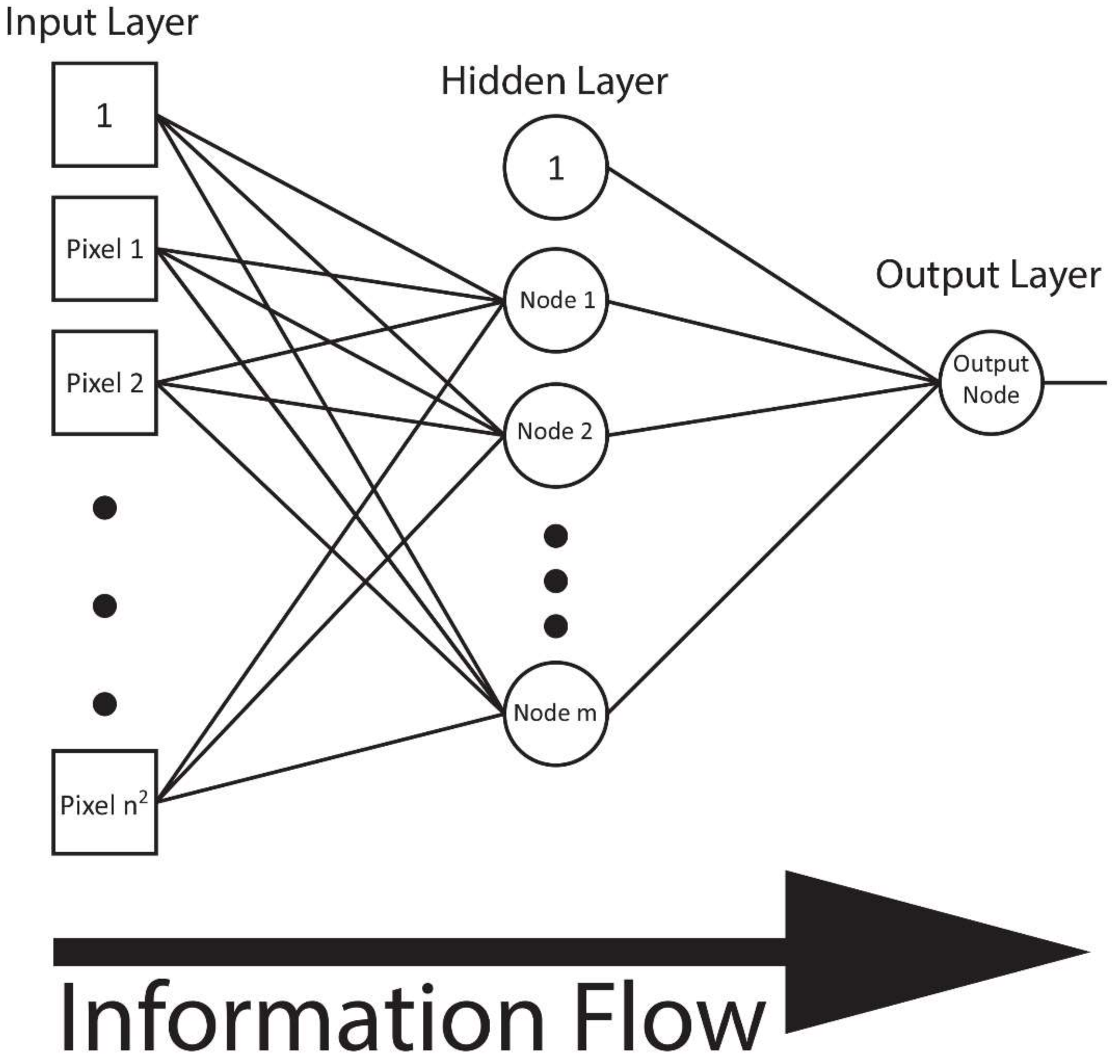
Input Layer
1
Pixel 1
Pixel 2
Pixel n^2
Hidden Layer
1
Node 1
Node 2
Node m
Output Layer
Output Node
Information Flow

FIGURE 4: This shows the general architecture of an artificial neural network using a single hidden layer. Pixel information is fed into each hidden neural node and the resulting values from each output node is fed into the output node. For both the input layer and the hidden layer the first value is a bias unit fixed to 1.

inherently parallelizable, and the solution can then be implemented by a massively parallelized approach on a graphical processing unit(GPU). Although the time required to measure the activation value of one pixel may be much longer than for other methods, parallelizing the problem accelerates the analysis by over an order of magnitude(overall), making the analysis of large data sets much more temporally economical on the GPU. This also has the advantage of using previously trained ANN parameters to get a real time estimation of data when this method is paired with a GPU based localization algorithm such as MLE[63].

A simulation was made to benchmark MINuTIA's performance. The simulation measured the distributions of experimental parameters images acquired from single color FPALM experiments fitted independently using a published localization analysis method[17]. Using these distributions(Figure 6), the simulation produced tens of thousands of simulated molecular images(Figure 7) distributed over ten thousand frames. The molecular images were simulated using the Gaussian PSF approximation whose height, width, position, and offset parameters were chosen to match simulation distributions. Different relative levels of heights and offsets were used to further test the limits of MINuTIA. The same neural architecture was used to analyze all the data sets. After identification, the regions were localized and the results were subjected to goodness of fit tolerances then compared to the known truths of the data sets.

3.3. Results

MINuTIA was performed on simulated files(Figure 7). The training was performed over multiple sets of random frames from the file. The results of the full localization analysis with

FIGURE 5 Performance Versus Hidden Layer Nodes

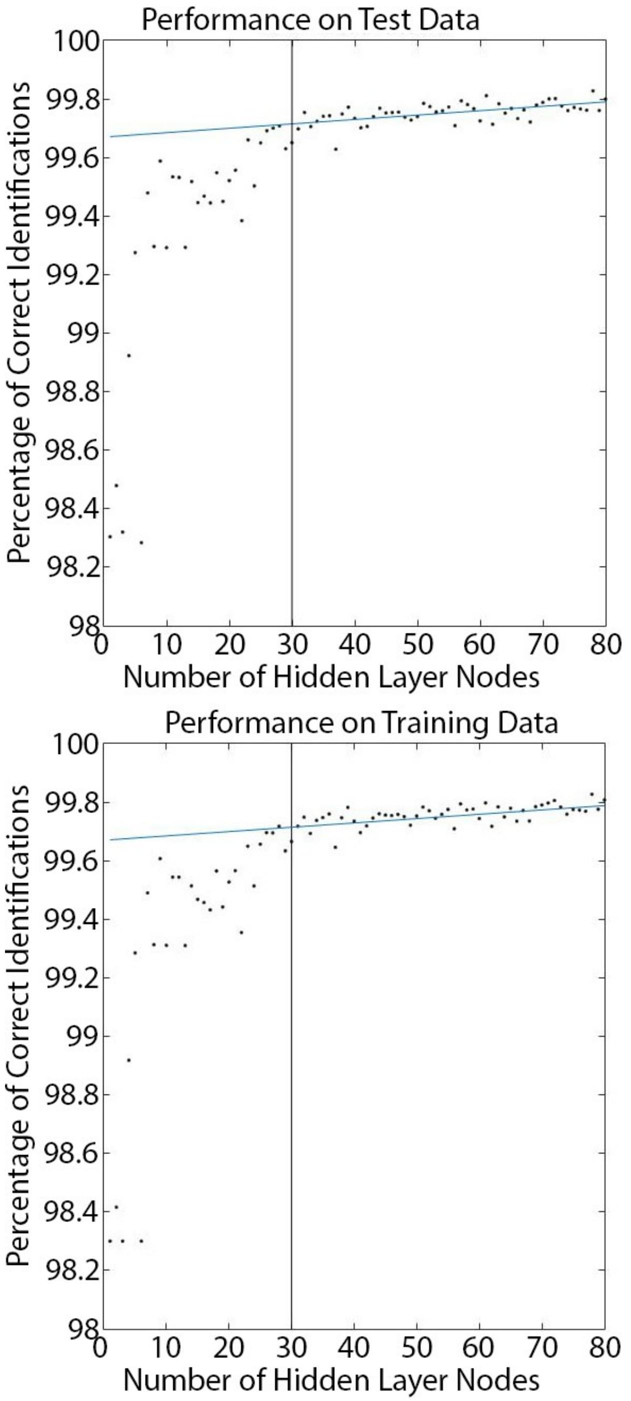

FIGURE 5: The results of identification accuracy on known data. The data was divided into two parts with 70% being used to train the neural network and 30% being used to test how well it performed on new data. This shows that after 30 nodes the improvement of the neural network's performance is greatly reduced which serves as a natural point for node selection.

each iteration of learned neural parameters were examined. We noticed that the detection accuracy(the percentage of identifications that match known truths before tolerances) rose very quickly to slightly above 95% in the non-astigmatism sets. False positives, defined as the percentage of false identifications compared to all identifications, quickly fell to values between 6-20%. After tolerances, the detection efficiency dropped to slightly above 90% while the false positive rate fell below 1%. After 18 iterations, the detection accuracy and false positive rates had stabilized to above 90% and below 0.6% respectively. For the astigmatism data set, the detection efficiency after tolerances was reduced to 80%, but the false positive rate stayed below 1%(Figure 8).

Of the molecules that were not detected there was a noticeable difference between the missed molecules and the ones detected. On average the number of expected photons was much lower for the missed molecules at 170 average photons than for the detected molecules at 230 photons on average. The average ratio of expected photons to the square root of the offset for the missing molecules was also lower at 69 than the average for the detected molecules at 73. This information indicates that the molecules that are missed are the ones that would result in poorer fits, and would be harder to confirm as molecules.

MINuTIA was again trained over multiple data sets containing different molecular brightness values(the total number of photons emitted from a molecule per camera frame). As the average brightness increases, detection accuracy remained above 90% while the false positive rate remains below 1%. There was no obvious advantage to using a training set comprised of homogenous molecules, in comparison to a training set that contained more heterogeneously distributed molecules. The final results for detection accuracy of the dimmest data set was still above 90% with less than 1% false positive identification(Figure 8A).

FIGURE 6 Example of Experimental and Simulated Histograms of Fitting Parameters

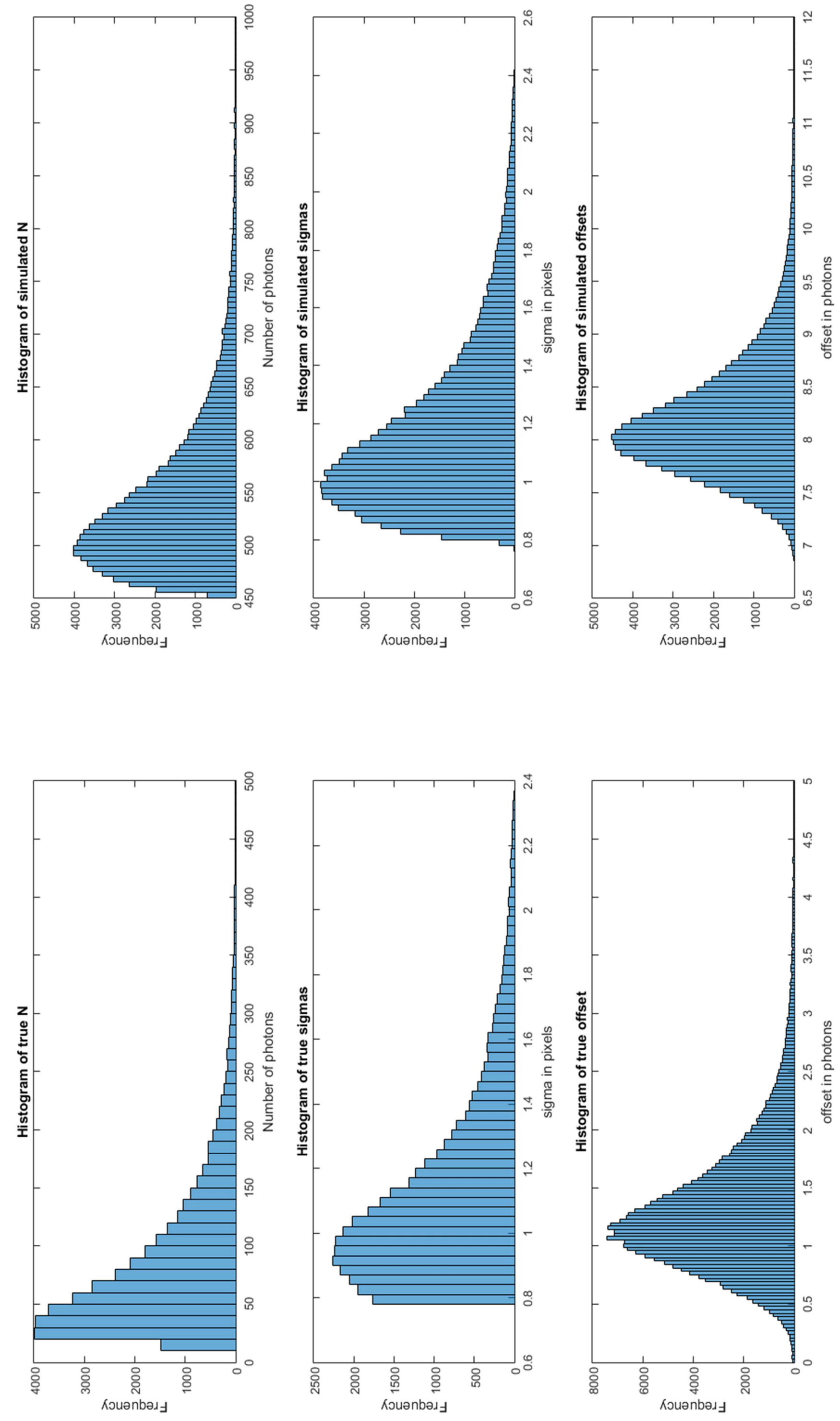

FIGURE 6: The distribution of Gaussian variables used to create the simulated data for benchmarking MINuTIA. The left column shows the distributions obtained from actual data from localization experiments. The right column shows the fabricate distributions used to in the simulation.

3.4. Discussion

The pixels of our camera have 16 bit resolution and can take on any value between 0 and 65355 ADU. For super resolution imaging it is essential that we not only avoid saturating one pixel, but also ensure we stay within the range of linear response of each pixel to photons. This often puts the maximal value a pixel will take on into the low 10s of thousands of ADU. We can think of all the pixels as mutually orthogonal unit vectors, and the pixel value as a scalar multiplier(i.e component in a particular unit vector direction). In this sense, all the images capable of being represented by a 7 pixel by 7 pixel area form a 49 dimensional hyperspace consisting of more than 10^{236} possible points or images. The task we attempt to accomplish is to define a multivariate function capable of mapping this high dimensionality vector space onto a binary output. While the true function may be impossible to know, multi-layered feed forward neural networks are well suited for approximating this function arbitrarily well [65].

Our simulations suggest that MINuTIA can be highly effective at selecting regions containing molecules while avoiding false positives, even in cases where the point spread function has been altered from its normal shape, such as with astigmatic detection. This is imperative for maximizing data fidelity, as well as minimizing analysis time. While the results of our simulations were highly promising, we can only use them as a prediction of the performance of MINuTIA on actual data, namely that MINuTIA is expected to be highly effective at learning to identify regions in an experimental data set that will result in a successful localization fit.

FIGURE 7 Examples of Simulated Data Sets

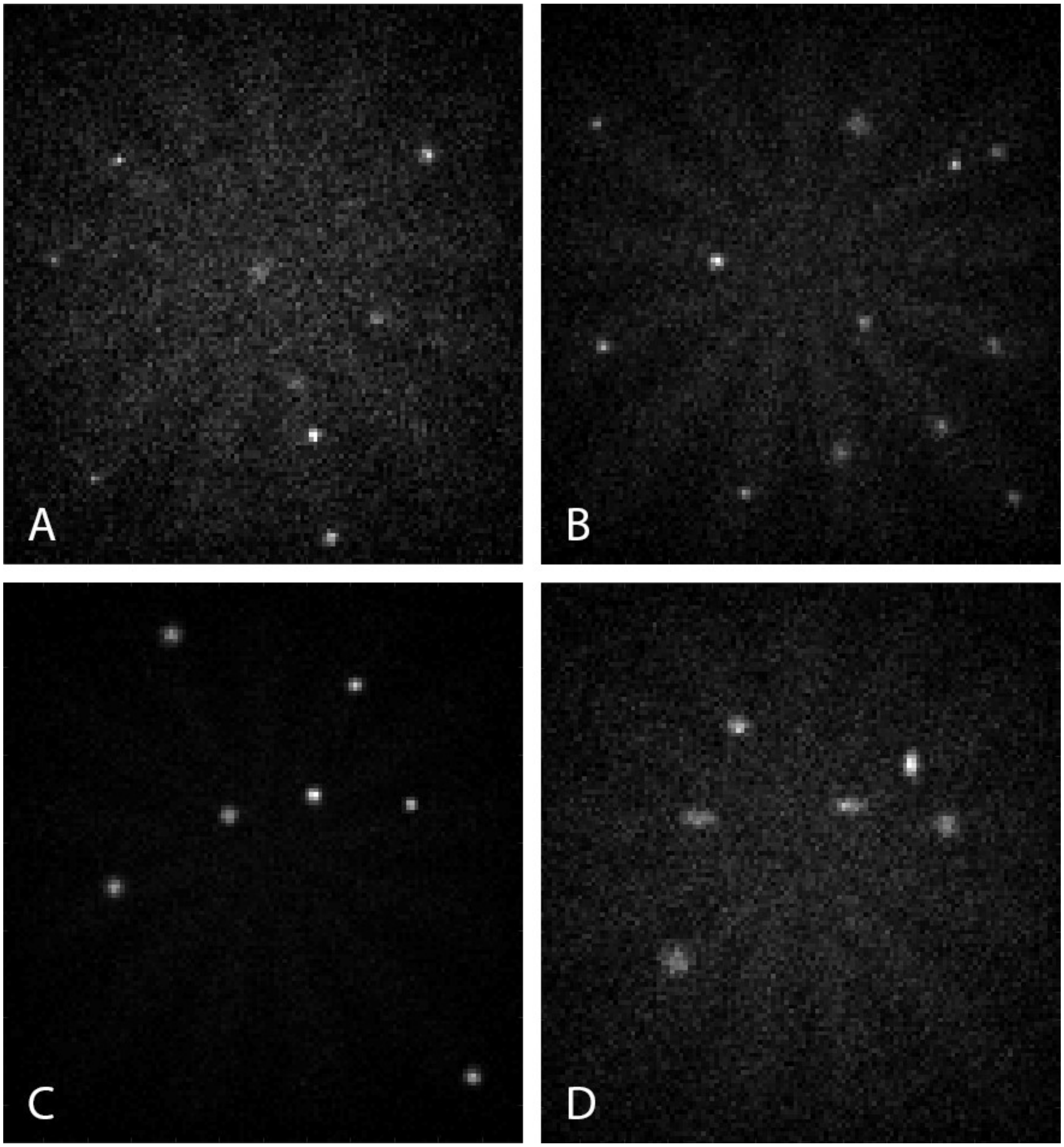

FIGURE 7: Representation of simulated data at different peak number of photons detected and different backgrounds. A) represents a low signal to noise example. B) Represents a relatively mid-range signal to noise example. C) Represents a high signal to noise ratio example. D) Represents an example of a data set with astigmatism images

In our simulations we see that MINuTIA can identify regions for fitting with up to a 90% success rate; however, in actual data we usually see success rates between 70% and 80%. We attribute this, in part, to our simulations not perfectly representing data acquisition, specifically the contribution of background to the data, the effect of molecular orientation on the final PSF, and defocusing of molecules near the focal plane. The success rate in the experimental data sets represents the percentage of regions that result in a good fit. Without additional information, and a far more elaborate experimental procedure, it is impossible to know the actual detection efficiency of an analyzed experimental data set.

We notice there is fluctuation in the success rate as iterations continue to increase. As the process is allowed to continue we see that the success rate plateaus within a window generally between 70 and 85% successful identification. We attribute this to the algorithm using different files and frames for each iteration. We make this identification based on the fact that we see significantly less fluctuation in the success rate on simulated data, and a much tighter plateau window. However on actual data there is much more cell to cell variability, which can have larger impacts on imaging conditions than the simulation accounted for. As background levels, fluorescent protein expression, and other variables fluctuate between cells, we expect to have some data sets with low background and easily localizable molecules, and some data sets with higher background and molecules that are more difficult to localize. We expect that this variation in data set conditions leads to the fluctuation in success rate seen with experimental data. To a much lesser extent there is some variation in success rate that arrives from how the training set images are handled. To avoid overloading the computer memory, we remove a percentage of images at random after each iteration. Without this step, the learning becomes progressively, and eventually prohibitively, slow. We have still seen the fluctuation in success

FIGURE 8 Results of Simulation

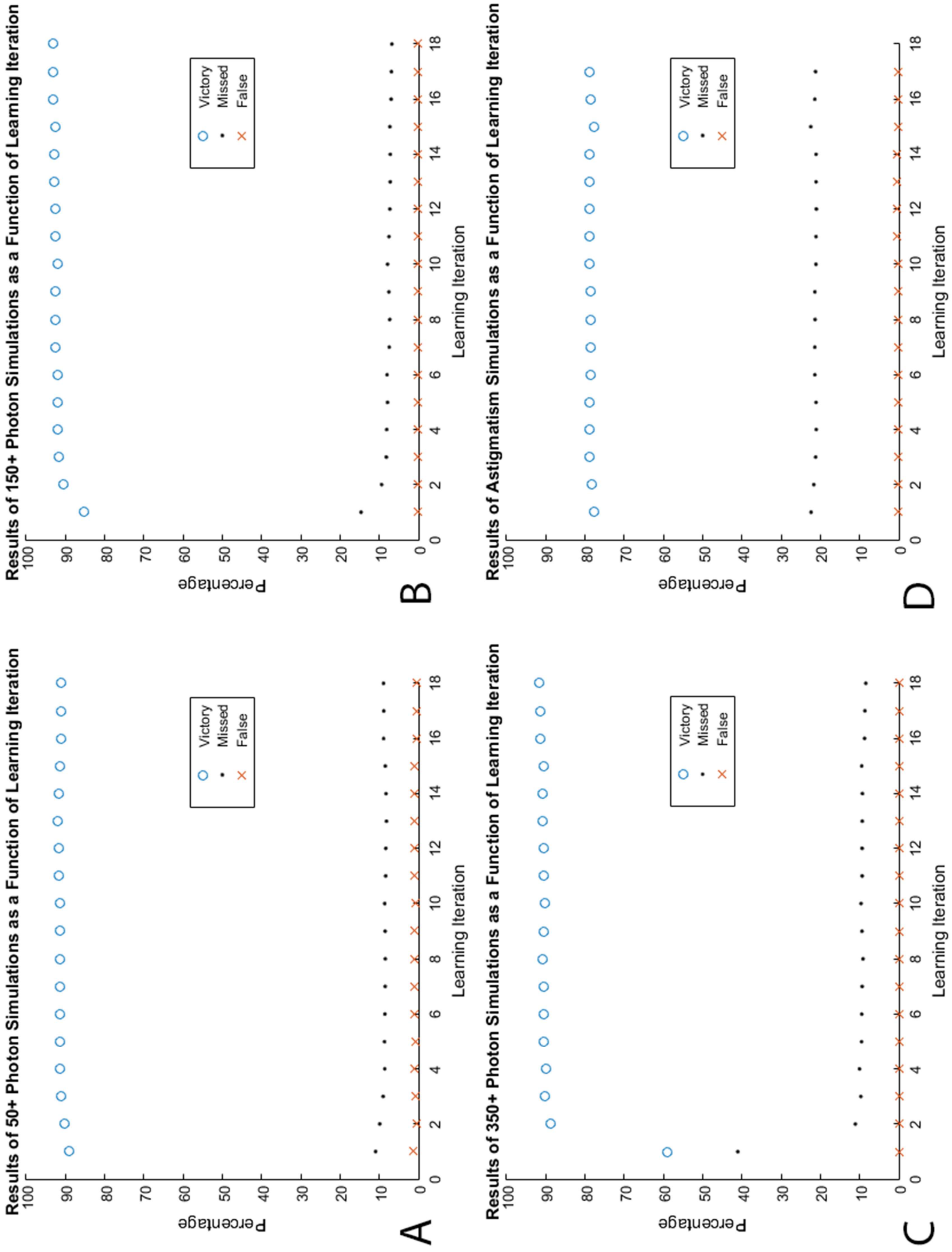

FIGURE 8: The results of the analyzed simulation data sets after tolerances have been applied as learning is iterated. A) Shows the results of the low signal to noise set B) Shows the results of the medium signal to noise set C) shows the results of the high signal to noise set. In these cases, the rate of finding molecules settled around 90% while the rates of false postives fell below 1%. D) Shows the results of learning on astigmatism data. Here the rate of finding molecules settled to just below 80% while the rate of false positives stayed below 1%

rate when we do not remove any images from the training set, but we acknowledge that by removing examples of ‘good’ and ‘bad’ molecules, the algorithm is altering the training, and thereby the success rate.

We noticed that within the first couple of iterations, MINuTIA becomes increasingly efficient at identifying molecules. After the 15th iteration, the efficiency suffers a bit. On this iteration we increase from 100 to 1000 frames. This is done to prevent the early iterations of the neural net from choosing too many non-specific regions which would make the process much slower than necessary. After this point we notice that MINuTIA quickly asymptotes to some value for percentage of successful fits of the total identifications. We also notice that the detection accuracy also asymptotes to some value above 80% for our simulations. The false positive rate also asymptotes much quicker and stays constantly low.

The MINuTIA algorithm has been demonstrated with a Gaussian fitting algorithm to learn what images will result in a ‘good’ fit and discriminate against regions that would not. However, this fitting algorithm is not necessary for the MINuTIA algorithm to perform, and in principle MINuTIA could be paired with any fitting algorithm to learn regions that would result in good fits versus those that would not. As such we posit that the MINuTIA algorithm is adaptable to any fitting function. This should allow MINuTIA to be incorporated into other localization experiments such as astigmatism, biplane, or experiments that involve point spread function shaping. To help speed up learning, test images of Gaussians were provided to MINuTIA early on in the process, analogously test images of the expected PSF could be provided for experiments where the PSF deviates significantly from a Gaussian approximation. The MINuTIA algorithm could potentially be used for analysis of localized data. The algorithm described uses assumptions about structure to speed up learning, but could be adapted to recognize any spatial pattern if MINuTIA is provided with a way to determine the success of a region.

3.5. Summary and Conclusion

Here we describe an artificial neural network which can learn the spatial pattern of a pixelated point spread function with a high degree of accuracy. This method allows for reduced user-induced bias in the identification process by allowing the MINuTIA algorithm to decide what spatial patterns are important for identification. This process also has an advantage over supervised artificial neural networks in that it can learn from its mistakes, which supervised neural networks cannot do as easily. Simulations show that this process is able to identify different patterns with no change to neural architecture. This suggests the MINuTIA process is a generalized molecular identification algorithm that could be used in experiments where manipulation of the point spread function is performed such as biplane or double-helix PSF imaging.

This technique further investigates the uses of artificial neural networks in localization microscopy, which help to combine a very powerful data science technique with a technique capable of producing massive amounts of data. Improvements to this technique could arise from investigating different neural network architectures including adding hidden layers, or convolutional layers, to the process, at the cost of development, learning, and computational time. Additionally this technique could potentially be paired with other localization algorithms such as multi-emitter fitting[15].

Using a robust identification algorithm could allow for the detection of molecules with lower signal to noise ratios, such as those seen in high speed imaging[1]. Incorporating this technique into high speed experimental designs would allow for a more reliable, faster final render than what has been previous presented. While this technique itself helps to deal with the issue of increased background and lowered signal, pairing it with a high density localization algorithm such as multi-emitter fitting[15] could allow for improved sampling on similar time scales, thus improving the overall spatial (or temporal) resolution.

High speed localization microscopy is still a developing technology with much promise. Improved temporal resolution in such techniques can offer answers to new questions about the nature of interaction between biomolecules, or reexamine established answers of stability in biostructures such as was shown in the second chapter. Optimization of localization techniques may also follow from incorporation of probe photophysics into experimental design considerations, from improved probes that are more suited for high speed imaging, and from showing that algorithms such as MINuTIA can be paired with high density localization algorithms to improve overall sampling of structures.

BIBLIOGRAPHY

1. Nelson, A.J., M.S. Gunewardene, and S.T. Hess. *High speed fluorescence photoactivation localization microscopy imaging*. 2014.

2. Hess, S.T., T.P.K. Girirajan, and M.D. Mason, *Ultra-high resolution imaging by fluorescence photoactivation localization microscopy.* Biophysical Journal, 2006. **91**(11): p. 4258-4272.

3. Betzig, E., et al., *Imaging intracellular fluorescent proteins at nanometer resolution.* Science, 2006. **313**(5793): p. 1642-1645.

4. Rust, M.J., M. Bates, and X.W. Zhuang, *Sub-diffraction-limit imaging by stochastic optical reconstruction microscopy (STORM).* Nature Methods, 2006. **3**(10): p. 793-795.

5. Huang, F., et al., *Video-rate nanoscopy using sCMOS camera-specific single-molecule localization algorithms.* Nature Methods, 2013. **10**(7): p. 653-658.

6. Gross, D. and W.W. Webb, *Molecular Counting of Low-Density Lipoprotein Particles as Individuals and Small Clusters on Cell Surfaces.* Biophysical Journal, 1986. **49**(4): p. 901-911.

7. Thompson, R.E., D.R. Larson, and W.W. Webb, *Precise nanometer localization analysis for individual fluorescent probes.* Biophysical Journal, 2002. **82**(5): p. 2775-2783.

8. Yildiz, A., et al., *Myosin V walks hand-over-hand: Single fluorophore imaging with 1.5-nm localization.* Science, 2003. **300**(5628): p. 2061-2065.

9. Dickson, R.M., et al., *On/off blinking and switching behaviour of single molecules of green fluorescent protein.* Nature, 1997. **388**(6640): p. 355-358.

10. Haupts, U., et al., *Dynamics of fluorescence fluctuations in green fluorescent protein observed by fluorescence correlation spectroscopy.* Proceedings of the National Academy of Sciences of the United States of America, 1998. **95**(23): p. 13573-13578.

11. Lippincott-Schwartz, J. and G.H. Patterson, *Photoactivatable fluorescent proteins for diffraction-limited and super-resolution imaging.* Trends in Cell Biology, 2009. **19**(11): p. 555-565.

12. Chudakov, D.M., et al., *Photoswitchable cyan fluorescent protein for protein tracking.* Nature Biotechnology, 2004. **22**(11): p. 1435-1439.

13. Enderlein, J., E. Toprak, and P.R. Selvin, *Polarization effect on position accuracy of fluorophore localization.* Optics Express, 2006. **14**(18): p. 8111-8120.

14. Holden, S.J., S. Uphoff, and A.N. Kapanidis, *DAOSTORM: an algorithm for high- density super-resolution microscopy.* Nature Methods, 2011. **8**(4): p. 279-280.

15. Huang, F., et al., *Simultaneous multiple-emitter fitting for single molecule super-resolution imaging.* Biomed Opt Express, 2011. **2**: p. 1377-1393.

16. Cox, S., et al., *Bayesian localization microscopy reveals nanoscale podosome dynamics.* Nature Methods, 2012. **9**(2): p. 195-200.

17. Hess, S.T., et al., *Dynamic clustered distribution of hemagglutinin resolved at 40 nm in living cell membranes discriminates between raft theories.* Proceedings of the National Academy of Sciences of the United States of America, 2007. **104**(44): p. 17370-17375.

18. Zacharias, D.A., et al., *Partitioning of Lipid-Modified Monomeric GFPs into Membrane Microdomains of Live Cells.* Science, 2002. **296**(5569): p. 913-916.

19. Dempsey, G.T., et al., *Evaluation of Fluorophores for Optimal Performance in Localization-Based Super-Resolution Imaging.* Nature Methods, 2011. **8**(12): p. 1027-1026.

20. Heilemann, M., et al., *Subdiffraction-resolution fluorescence imaging with conventional fluorescent probes.* Angewandte Chemie-International Edition, 2008. **47**(33): p. 6172-6176.

21. Linde, S., et al., *Photoswitching microscopy with standard fluorophores.* Applied Physics B, 2008. **93**(4): p. 725-731.

22. Shim, S.-H., et al., *Super-resolution fluorescence imaging of organelles in live cells with photoswitchable membrane probes.* Proceedings of the National Academy of Sciences, 2012. **109**(35): p. 13978-13983.

23. Jones, S.A., et al., *Fast, three-dimensional super-resolution imaging of live cells.* Nature Methods, 2011. **8**(6): p. 499-505.

24. Zessin, P.J.M., K. Finan, and M. Heilemann, *Super-resolution fluorescence imaging of chromosomal DNA.* Journal of Structural Biology, 2012. **177**(2): p. 344-348.

25. Xu, J., et al., *Labeling Cytosolic Targets in Live Cells with Blinking Probes.* The Journal of Physical Chemistry Letters, 2013. **4**(13): p. 2138-2146.

26. Wilmes, S., et al., *Triple-Color Super-Resolution Imaging of Live Cells: Resolving Submicroscopic Receptor Organization in the Plasma Membrane.* Angewandte Chemie International Edition, 2012. **51**(20): p. 4868-4871.

27. Appelhans, T., et al., *Nanoscale Organization of Mitochondrial Microcompartments Revealed by Combining Tracking and Localization Microscopy.* Nano Letters, 2011. **12**(2): p. 610-616.

28. Los, G.V., et al., *HaloTag: A Novel Protein Labeling Technology for Cell Imaging and Protein Analysis.* ACS Chemical Biology, 2008. **3**(6): p. 373-382.

29. Gould, T.J., et al., *Nanoscale imaging of molecular positions and anisotropies.* Nature Methods, 2008. **5**(12): p. 1027-1030.

30. Manley, S., et al., *High-density mapping of single-molecule trajectories with photoactivated localization microscopy.* Nature Methods, 2008. **5**(2): p. 155-157.

31. Shtengel, G., et al., *Interferometric fluorescent super-resolution microscopy resolves 3D cellular ultrastructure.* Proceedings of the National Academy of Sciences of the United States of America, 2009. **106**(9): p. 3125-3130.

32. Shroff, H., et al., *Dual-color superresolution imaging of genetically expressed probes within individual adhesion complexes.* Proceedings of the National Academy of Sciences of the United States of America, 2007. **104**(51): p. 20308-20313.

33. Bock, H., et al., *Two-color far-field fluorescence nanoscopy based on photoswitchable emitters.* Applied Physics B-Lasers and Optics, 2007. **88**(2): p. 161-165.

34. Andresen, M., et al., *Photoswitchable fluorescent proteins enable monochromatic multilabel imaging and dual color fluorescence nanoscopy.* Nature Biotechnology, 2008. **26**(9): p. 1035-1040.

35. Bates, M., et al., *Multicolor super-resolution imaging with photo-switchable fluorescent probes.* Science, 2007. **317**(5845): p. 1749-1753.

36. Gunewardene, Mudalige S., et al., *Superresolution Imaging of Multiple Fluorescent Proteins with Highly Overlapping Emission Spectra in Living Cells.* Biophysical Journal, 2011. **101**(6): p. 1522-1528.

37. Bossi, M., et al., *Multicolor far-field fluorescence nanoscopy through isolated detection of distinct molecular species.* Nano Letters, 2008. **8**(8): p. 2463-2468.

38. Folling, J., et al., *Fluorescence nanoscopy by ground-state depletion and single-molecule return.* Nature Methods, 2008. **5**(11): p. 943-945.

39. Subach, F.V., et al., *Photoactivatable mCherry for high-resolution two-color fluorescence microscopy.* Nature Methods, 2009. **6**(2): p. 153-159.

40. Huang, B., et al., *Three-dimensional super-resolution imaging by stochastic optical reconstruction microscopy.* Science, 2008. **319**(5864): p. 810-813.

41. Juette, M.F., et al., *Three-dimensional sub-100 nm resolution fluorescence microscopy of thick samples.* Nature Methods, 2008. **5**(6): p. 527-529.

42. Xu, K., H.P. Babcock, and X. Zhuang, *Dual-objective STORM reveals three-dimensional filament organization in the actin cytoskeleton.* Nat Meth, 2012. **9**(2): p. 185-188.

43. Pavani, S.R.P., et al., *Three-dimensional, single-molecule fluorescence imaging beyond the diffraction limit by using a double-helix point spread function.* Proceedings of the

National Academy of Sciences of the United States of America, 2009. **106**(9): p. 2995-2999.

44. Nieuwenhuizen, R.P.J., et al., *Measuring image resolution in optical nanoscopy.* Nature Methods, 2013. **10**(6): p. 557-562.

45. Pertsinidis, A., Y. Zhang, and S. Chu, *Subnanometre single-molecule localization, registration and distance measurements.* Nature Methods, 2010. **466**(7306): p. 647-651.

46. Mlodzianoski, M.J., et al., *Sample drift correction in 3D fluorescence photoactivation localization microscopy.* Optics Express, 2011. **19**(16): p. 15009-15019.

47. Backlund, M.P., et al., *Simultaneous, accurate measurement of the 3D position and orientation of single molecules.* Proceedings of the National Academy of Sciences, 2012.

48. Takeda, M., et al., *Influenza virus hemagglutinin concentrates in lipid raft microdomains for efficient viral fusion.* Proceedings of the National Academy of Sciences of the United States of America, 2003. **100**(25): p. 14610-14617.

49. Shaw, M.L., et al., *Cellular proteins in influenza virus particles.* Plos Pathogens, 2008. **4**(6).

50. Schwille, P., et al., *Fluorescence correlation spectroscopy reveals fast optical excitation-driven intramolecular dynamics of yellow fluorescent proteins.* Proceedings of the National Academy of Sciences, 2000. **97**(1): p. 151-156.

51. Hell, S. and E.H.K. Stelzer, *Fundamental Improvement of Resolution with a 4pi-Confocal Fluorescence Microscope Using 2-Photon Excitation.* Optics Communications, 1992. **93**(5-6): p. 277-282.

52. Tokunaga, M., N. Imamoto, and K. Sakata-Sogawa, *Highly inclined thin illumination enables clear single-molecule imaging in cells.* Nat Meth, 2008. **5**(2): p. 159-161.

53. Konopka, C.A. and S.Y. Bednarek, *Variable-angle epifluorescence microscopy: a new way to look at protein dynamics in the plant cell cortex.* The Plant Journal, 2008. **53**(1): p. 186-196.

54. Huisken, J., et al., *Optical Sectioning Deep Inside Live Embryos by Selective Plane Illumination Microscopy.* Science, 2004. **305**(5686): p. 1007-1009.

55. Shroff, H., et al., *Live-cell photoactivated localization microscopy of nanoscale adhesion dynamics.* Nat Meth, 2008. **5**(5): p. 417-423.

56. Banterle, N., et al., *Fourier ring correlation as a resolution criterion for super-resolution microscopy.* Journal of Structural Biology, 2013. **183**(3): p. 363-367.

57. Mukamel, E.A. and M.J. Schnitzer, *Unified Resolution Bounds for Conventional and Stochastic Localization Fluorescence Microscopy.* Physical Review Letters, 2012. **109**(16): p. 168102.

58. Betzig, E., et al., *Imaging Intracellular Fluorescent Proteins at Nanometer Resolution.* Science, 2006. **313**(5793): p. 1642.

59. Rust, M.J., M. Bates, and X. Zhuang, *Sub-diffraction-limit imaging by stochastic optical reconstruction microscopy (STORM).* Nat Meth, 2006. **3**(10): p. 793-796.

60. Smith, C.S., et al., *Probability-based particle detection that enables threshold-free and robust in vivo single-molecule tracking.* Molecular Biology of the Cell, 2015. **26**(22): p. 4057-4062.

61. Olivo-Marin, J.-C., *Extraction of spots in biological images using multiscale products.* Pattern Recognition, 2002. **35**(9): p. 1989-1996.

62. Serge, A., et al., *Dynamic multiple-target tracing to probe spatiotemporal cartography of cell membranes.* Nat Meth, 2008. **5**(8): p. 687-694.

63. Smith, C.S., et al., *Fast, single-molecule localization that achieves theoretically minimum uncertainty.* Nat Meth, 2010. **7**(5): p. 373-375.

64. Izeddin, I., et al., *Wavelet analysis for single molecule localization microscopy.* Optics Express, 2012. **20**(3): p. 2081-2095.

65. Hornik, K., M. Stinchcombe, and H. White, *Multilayer feedforward networks are universal approximators.* Neural Networks, 1989. **2**(5): p. 359-366.

66. Cheng, B. and D.M. Titterington, *Neural Networks: A Review from a Statistical Perspective.* 1994: p. 2-30.

67. Rumelhart, D.E., G.E. Hinton, and R.J. Williams, *Learning representations by back-propagating errors.* Nature, 1986. **323**(6088): p. 533-536.

68. Gould, T.J., V.V. Verkhusha, and S.T. Hess, *Imaging biological structures with fluorescence photoactivation localization microscopy.* Nat. Protocols, 2009. **4**(3): p. 291-308.

69. Cybenko, G., *Approximation by superpositions of a sigmoidal function.* Mathematics of Control, Signals and Systems, 1989. **2**(4): p. 303-314.

70. Rumelhart, D.E., G.E. Hinton, and R.J. Williams, *Parallel Distributed Processing: Explorations in the Microstructure of Cognition*. 1986.

71. Curthoys, N.M., et al., *Chapter Three - Dances with Membranes: Breakthroughs from Super-resolution Imaging*, in *Current Topics in Membranes*, K.K. Anne, Editor. 2015, Academic Press. p. 59-123.

72. Manes, S., G. del Real, and C. Martinez, *Pathogens: Raft Hijackers.* Nature Reviews Immunology, 2003. **3**: p. 557-568.

73. Ruigrok, R.W.H., et al., *Natural heterogeneity of shape, infectivity and protein composition in an influenza A (H3N2) virus preparation.* Virus Research, 1985. **3**(1): p. 69-76.

74. Hess, S.T., et al., *Quantitative electron microscopy and fluorescence spectroscopy of the membrane distribution of influenza hemagglutinin.* The Journal of Cell Biology, 2005. **169**(6): p. 965.

75. Engel, S., et al., *FLIM-FRET and FRAP reveal association of influenza virus haemagglutinin with membrane rafts.* Biochemical Journal, 2010. **425**(3): p. 567-73.

76. Karpova, T.S., et al., *Fluorescence resonance energy transfer from cyan to yellow fluorescent protein detected by acceptor photobleaching using confocal microscopy and a single laser.* Journal of Microscopy-Oxford, 2003. **209**: p. 56-70.

77. Kenworthy, A.K., *Imaging protein-protein interactions using fluorescence resonance energy transfer microscopy.* Methods, 2001. **24**(3): p. 289-296.

78. Kenworthy, A.K., *Fleeting glimpses of lipid rafts: How biophysics is being used to track them.* Journal of Investigative Medicine, 2005. **53**(6): p. 312-317.

79. Kenworthy, A.K. and M. Edidin, *Distribution of a glycosylphosphatidylinositol-anchored protein at the apical surface of MDCK cells examined at a resolution of < 100 angstrom using imaging fluorescence resonance energy transfer.* Journal of Cell Biology, 1998. **142**(1): p. 69-84.

80. Kenworthy, A.K., N. Petranova, and M. Edidin, *High-resolution FRET microscopy of cholera toxin B-subunit and GPI-anchored proteins in cell plasma membranes.* Molecular Biology of the Cell, 2000. **11**(5): p. 1645-1655.

81. Elson, E.L., et al., *Measurement of lateral transport on cell surfaces.* Progress in Clinical and Biological Research, 1976. **9**: p. 137-47.

82. Kenworthy, A.K., et al., *Dynamics of putative raft-associated proteins at the cell surface.* Journal of Cell Biology, 2004. **165**(5): p. 735-746.

83. Polozov, I.V., et al., *Progressive ordering with decreasing temperature of the phospholipids of influenza virus.* Nat Chem Biol, 2008. **4**(4): p. 248-255.

84. Gudheti, M.V., et al., *Actin mediates the nanoscale membrane organization of the clustered membrane protein influenza hemagglutinin.* Biophys J, 2013. **104**(10): p. 2182-92.

85. Skehel, J.J. and D.C. Wiley, *Receptor binding and membrane fusion in virus entry: The influenza hemagglutinin.* Annual Review of Biochemistry, 2000. **69**: p. 531-569.

86. Biswas, S., et al., *Cholesterol promotes hemifusion and pore widening in membrane fusion induced by influenza hemagglutinin.* Journal of General Physiology, 2008. **131**(5): p. 503-513.

87. Chernomordik, L.V., et al., *The pathway of membrane fusion catalyzed by influenza hemagglutinin: Restriction of lipids, hemifusion, and lipidic fusion pore formation.* Journal of Cell Biology, 1998. **140**(6): p. 1369-1382.

88. Skehel, J.J. and D.C. Wiley, *Influenza haemagglutinin.* Vaccine, 2002. **20**: p. S51-S54.

89. Wiley, D.C. and J.J. Skehel, *The Structure and Function of the Hemagglutinin Membrane Glycoprotein of Influenza-Virus.* Annual Review of Biochemistry, 1987. **56**: p. 365-394.

90. Bentz, J., *Minimal aggregate size and minimal fusion unit for the first fusion pore of influenza hemagglutinin-mediated membrane fusion.* Biophysical Journal, 2000. **78**(1): p. 227-245.

91. Chernomordik, L.V., et al., *An early stage of membrane fusion mediated by the low pH conformation of influenza hemagglutinin depends upon membrane lipids.* Journal of Cell Biology, 1997. **136**(1): p. 81-93.

92. Kozlov, M.M. and L.V. Chernomordik, *A mechanism of protein-mediated fusion: Coupling between refolding of the influenza hemagglutinin and lipid rearrangements.* Biophysical Journal, 1998. **75**(3): p. 1384-1396.

93. Kumar, M., et al., *Raft association plays an important role in Influenza Hemagglutinin-mediated fusion.* Molecular Biology of the Cell, 2001. **12**: p. 74A-74A.

94. Nayak, D.P., E.K. Hui, and S. Barman, *Assembly and budding of influenza virus.* Virus Res, 2004. **106**(2): p. 147-65.

95. Scheiffele, P., et al., *Influenza viruses select ordered lipid domains during budding from the plasma membrane.* Journal of Biological Chemistry, 1999. **274**(4): p. 2038-2044.

96. Scheiffele, P., M.G. Roth, and K. Simons, *Interaction of influenza virus haemagglutinin with sphingolipid-cholesterol membrane domains via its transmembrane domain.* Embo Journal, 1997. **16**(18): p. 5501-5508.

97. Babcock, H.P., C. Chen, and X. Zhuang, *Using Single-Particle Tracking to Study Nuclear Trafficking of Viral Genes.* Biophysical Journal, 2004. **87**(4): p. 2749-2758.

98. Lakadamyali, M., et al., *Visualizing infection of individual influenza viruses.* Proceedings of the National Academy of Sciences of the United States of America, 2003. **100**(16): p. 9280-9285.

99. He, J., et al., *Dual Function of CD81 in Influenza Virus Uncoating and Budding.* PLoS Pathog, 2013. **9**(10): p. e1003701.

100. Rocha-Perugini, V., M. Gordon-Alonso, and F. Sanchez-Madrid, *PIP2: choreographer of actin-adaptor proteins in the HIV-1 dance.* Trends Microbiol, 2014. **22**(7): p. 379-88.

101. Berditchevski, F., *Complexes of tetraspanins with integrins: more than meets the eye.* Journal of Cell Science, 2001. **114**(23): p. 4143.

102. Radtke, K., K. Döhner, and B. Sodeik, *Viral interactions with the cytoskeleton: a hitchhiker's guide to the cell.* Cellular Microbiology, 2006. **8**(3): p. 387-400.

103. Lingappa, J.R., et al., *How HIV-1 Gag assembles in cells: Putting together pieces of the puzzle.* Virus Research, 2014. **193**: p. 89-107.

104. Jouvenet, N., et al., *Plasma Membrane Is the Site of Productive HIV-1 Particle Assembly.* PLoS Biol, 2006. **4**(12): p. e435.

105. Roy, N.H., et al., *Clustering and Mobility of HIV-1 Env at Viral Assembly Sites Predict Its Propensity To Induce Cell-Cell Fusion.* Journal of Virology, 2013. **87**(13): p. 7516-7525.

106. Chojnacki, J., et al., *Maturation-Dependent HIV-1 Surface Protein Redistribution Revealed by Fluorescence Nanoscopy.* Science, 2012. **338**(6106): p. 524.

107. Chen, A.K., et al., *MicroRNA binding to the HIV-1 Gag protein inhibits Gag assembly and virus production.* Proceedings of the National Academy of Sciences, 2014. **111**(26): p. E2676-E2683.

108. Grover, J.R., S.L. Veatch, and A. Ono, *Basic Motifs Target PSGL-1, CD43, and CD44 to Plasma Membrane Sites Where HIV-1 Assembles.* Journal of Virology, 2015. **89**(1): p. 454-467.

109. Van Engelenburg, S.B., et al., *Distribution of ESCRT Machinery at HIV Assembly Sites Reveals Virus Scaffolding of ESCRT Subunits.* Science, 2014. **343**(6171): p. 653.

110. Liu, L., et al., *From Crescent to Mature Virion: Vaccinia Virus Assembly and Maturation.* Viruses, 2014. **6**(10): p. 3787.

111. Stahelin, R.V., *Could the Ebola virus matrix protein VP40 be a drug target?* Expert Opinion on Therapeutic Targets, 2014. **18**(2): p. 115-120.

112. Gabor, K.A., et al., *Super Resolution Microscopy Reveals that Caveolin-1 Is Required for Spatial Organization of CRFB1 and Subsequent Antiviral Signaling in Zebrafish.* PLoS ONE, 2013. **8**(7): p. e68759.

113. Gabor, K.A., et al., *Nanoscale Imaging of Caveolin-1 Membrane Domains <italic>In Vivo</italic>.* PLoS ONE, 2015. **10**(2): p. e0117225.

APPENDIX A: VIRUS INFECTION

The following appendix is reproduced from a section of a published chapter by Curthoys et. al 2015[71].

Viruses are responsible worldwide for significant illness across many species, and are able to induce changes in the organization of the plasma membrane to facilitate infection, replication, budding, release, and evasion of the host immune system[72]. Exceptionally high resolution views of virus infection have been obtained with EM. For example, images of whole influenza virus[73] and in particular the influenza fusion protein hemagglutinin (HA)[74] have been obtained and quantified by EM. While not yet rivaling the resolution obtained by EM, super-resolution microscopy is far better suited for imaging living, dynamic systems. Coupled with advances in temporal resolution[1, 5], super-resolution imaging gives investigators the tools capable of answering more questions about pathogen interactions with host cell membranes. Because this is a highly researched field, were here limit discussion to a small subset of studies only.

A.1. Super-Resolution Microscopy: Viruses Meet Their Match

Even though direct optical imaging of membrane domains with diffraction limited techniques is not always possible, many properties of viral assembly and function can be uncovered through indirect imaging methods. FRET microscopy has reported the association between viral proteins and putative lipid raft markers[75], and FRET has been quite useful in quantifying clustering of many membrane proteins on length scales <10 nm[76-80]. FRAP[81] has yielded insight into mechanisms of diffusion of viral membrane proteins at the cell membrane[82], and nuclear magnetic resonance (NMR) has revealed how lipid phase changes as a function of temperature help protect viral stability[83]. However, FRET is insensitive to length scales from ~10 to 200 nm, NMR does not provide an image, and FRAP does not give direct information about spatial organization below the diffraction limit. Using super-resolution imaging, investigators have been able to directly quantify shapes, sizes, and densities of membrane protein distributions, as well as the degree of spatial overlap between different species of proteins at the nanoscale[17, 29, 32, 36, 84]. These capabilities have allowed researchers to answer previously inaccessible questions about viral assembly, viral protein trafficking, and viral interactions with host cell components, which help build our understanding of the infection process, and have the potential to reveal new anti-viral drug targets.

A.2. Influenza Virus Hemagglutinin: The Versatile Membrane Protein Hijacking Your Cells

The influenza virus is responsible for tens of thousands of deaths annually. Influenza can use host cell proteins to aid in infection, and mass spectrometry has shown that a number of host cell proteins are also preferentially incorporated into influenza virus released from infected cells[49], leading to the question of how these associations occur. Some answers may be found with the influenza membrane protein hemagglutinin (HA), which is crucial in many steps of viral infection. HA binds sialic-acid containing cell surface receptors[85]; HA catalyzes membrane fusion necessary for viral entry[85-89]; and clustering of HA in the viral membrane is crucial for fusion to be accomplished[48, 87, 90-93]. HA assembles with other viral components before budding[94], and in the late 1990s, biochemical experiments were able to show that the influenza virus buds from areas of the host membrane where viral components including HA and certain cell lipids are concentrated[95, 96]. HA dynamics have been investigated with SPT, which helped elucidate the HA-dependent mechanism by which viral RNA traverses the nuclear envelope[97, 98], and FRAP experiments measured the diffusion coefficient of HA ~0.1 $\mu m^2/s$, and suggested an immobile fraction (~25%) of HA[82]. While these experiments have greatly helped shape our understanding of influenza infection, they have not fully clarified the nanoscale organization of viral and host cell components during infection.

Recently, super-resolution experiments have made substantial advances in the understanding of several aspects of the influenza virus life cycle. Super-resolution microscopy has also been used to determine the spatial distribution of the host cell protein CD81 (tetraspanin), which is recruited to assembling influenza viruses, and is concentrated at the growing tip and budding neck of progeny viruses[99]. CD81 can control the progression of membrane protein distributions in, for example, immunological synapse formation[100], and form complexes with a number of signaling proteins and other master regulators such as the integrins[101]. Tetraspanin redistribution by influenza may be one method by which the virus is able to reorganize other host cell membrane proteins on the surface of budding virions.

A.3. Influenza Hemagglutinin and Host Cell Actin: An Unhealthy Relationship?

One other host cell protein which is greatly exploited by influenza, and viruses in general, is actin[102]. While it was shown that HA clusters (which are necessary precursors of viral budding[96]) can persist over timescales of at least tens of seconds[17], high-speed FPALM showed that fluctuations in area, perimeter, and shape of these clusters can occur on timescales as short as 0.1 s[1] leading to the question of how clusters are able to persist. Multicolor FPALM imaging in live cells has shown that HA mobility decreases with increased cortical actin density. Along with the discovery of two distinct populations of HA, one with low (non-zero) mobility and confined motion on 100–200 nm length scales[84], these findings suggest that local actin is influencing the dynamics of this membrane protein. Colocalization of HA clusters with actin clusters and the increase in HA cluster size upon treatment with actin-stabilizing jasplakinolide treatment do not seem consistent with a picket-fence description[84]. Moreover, the intriguing nanoscale differential anti- and colocalization of HA and ABPs, including cofilin (which is strikingly excluded from some HA clusters, yet strongly colocalizes with others), suggests the relationship is more involved than HA molecules simply being confined between actin fences[84]. Rather, these insights made possible by super-resolution microscopy suggest a dynamic “cluster feedback” between membrane HA and the underlying actin cytoskeleton. Understanding these HA organizing mechanisms could be vital in identifying novel antiviral drug treatments, and understanding the HA/actin/ABP interplay may illuminate cellular processes which are used to organize the distributions of many other membrane proteins.

A.4. Role of Gag in HIV Life Cycle

The U.S. Centers for Disease Control (CDC) estimates that the Human Immunodeficiency Virus (HIV) infects tens of thousands of people in the United States each year. Understanding of the molecular dynamics involved in HIV infection and replication is critical for developing future medical treatments for infected individuals, as well as for preventing infection. Formation of the HIV immature capsid (and in turn budding, release, and maturation of the virus) depends on formation of a polyprotein assembly of the HIV protein group-specific antigen (Gag)[103]. Live cell sptPALM was used to compare the dynamic behaviors of Gag and the vesicular stomatitis virus (VSV) G protein[30]. This allowed researchers to build dense “trajectory maps” of many different proteins to help understand the dynamic behavior of individual proteins, and entire populations and assemblies, in the plasma membrane. While the distributions and mobility of Gag and VSV-G proteins differed greatly, they were both found to be consistent with results obtained through diffraction-limited techniques[82, 104]. Using STORM, researchers revealed that Gag recruits and corrals the HIV viral envelope protein (Env) into large immobile clusters on the plasma membrane, in a process dependent on the Env cytoplasmic tail[105]. STED has also elucidated this relationship, revealing that clustering of Env on viral envelopes changed as a function of viral maturity, and that this clustering required the Gag-interacting Env tail[106]. Using sptPALM and PALM images, micro-RNA overexpression was shown to reduce Gag mobility, and also reduce Gag cluster size and density[107], which could in turn affect the clustering of HIV-1 Env and overall infectivity of the virus.

Multicolor super-resolution studies indicate that Gag colocalizes with a variety of host cell transmembrane proteins by interacting with basic motifs within their cytoplasmic tails[108]. Correlative iPALM/EM images and multicolor 3D super-resolution imaging have beautifully shown host cell endosomal sorting complexes required for transport (ESCRT) machinery bundled up inside the Gag lattice of budding virus particles[109], indicating that after hijacking ESCRT to help bud the host cell membrane, HIV virions swallow ESCRT whole.

A.5. Outlook

Ground-breaking progress in our understanding of virus infection has already emerged from the use of super-resolution microscopy. In particular, the manipulation of host membrane protein organization by viruses has been shown, at the nanoscale, to be imperative for some steps in viral infection. These microscopy methods could also be employed to help understand currently unknown mechanisms in past and rising health threats such as pox viruses (e.g., smallpox and vaccinia), coronaviruses (e.g., SARS), and filoviruses (e.g., Ebola and Marburg viruses). There are at least six membrane proteins known to be associated with the currently unclear process of virion formation in the vaccinia virus[110]. In filoviruses, the proteins responsible for viral assembly and virion production have been identified, but the mechanisms of interaction with the host cell remain unclear[111]. Understanding the interplay between host and viral membrane protein organization at the nanoscale with super-resolution microscopy will undoubtedly continue to rapidly improve our understanding of virus infection, and so aid in the development of targeted and efficacious antiviral therapies. Super-resolution microscopy has also been used to study the defenses mounted by cells upon viral. FPALM imaging of zebrafish cells showed that snakehead rhabdovirus (SHRV) infection resulted in downregulated caveolin expression, which in turn dispersed the clustering of a zebrafish type I interferon receptor (IFN-R) homolog, the clustering of which was crucial for the innate immune response[112]. Exciting recent developments now show that FPALM can be used in vivo to image membrane structures within living zebrafish[113], suggesting that changes in membrane organization during viral infection, and many other possibilities, can now be investigated in vivo.

Many super-resolution viral studies have focused on assembly and related processes near the membrane. While these experiments provide invaluable information about the viral life cycle, they explore only a part of the full story. More research into the organization and dynamics of the virion envelope during binding, entry, and uncoating, could provide additional insights and help identify new antiviral drug targets. As many entire virions can be smaller than the diffraction limit, questions relating to the organization of host cell and viral proteins within the virion itself require the ability to image nanoscale structure. Super-resolution can see at the nano- and virus-scale, and we can now resolve host cell proteins (and lipids) in living cells as they are commandeered by the virus. These capabilities are well suited for understanding infection, so we can better develop methods to combat it. We look forward to seeing in real time at the nanoscale exactly how viruses use, abuse, and steal our membranes and associated proteins for their own infective purposes.

BIOGRAPHY OF THE AUTHOR

Andrew J. Nelson was born in Falls Church, Virginia on May 3, 1986. He was raised in Fairfax, Virginia and graduated from the W. T. Woodson High School in 2005. He attended the College of William and Mary and graduated in 2009 with a Bachelor's of science degree in Physics. He entered the Physics and Astronomy graduate program at the University of Maine in the fall of 2010. Andrew is a candidate for the Doctor of Philosophy degree in Physics from the University of Maine in December 2016.